Available online at www.sciencedirect.com
ScienceDirect
Trans. Nonferrous Met. Soc. China 34(2024) 480−503
Transactions of Nonferrous Metals Society of China
www.tnmsc.cn

Recrystallization behavior and strengthening mechanism of extruded Mg−Gd−Y−Zn−Zr alloy with different pre-aged states

Jian XU[1], Jie ZHENG[1], Wan-er LIU[2], You-wang HUANG[3],
Zhao-ming YAN[1], Zhi-min ZHANG[1], Qiang WANG[1], Yong XUE[1]

1. School of Materials Science and Engineering, North University of China, Taiyuan 030051, China;
2. Beijing Institute of Astronautical Systems Engineering, Beijing 100076, China;
3. Beijing Institute of Space Long March Vehicle, Beijing 100071, China

Received 7 June 2022; accepted 16 December 2022

Abstract: Three different samples were prepared by tailoring the pre-ageing time to investigate the effect of different pre-aged states on the dynamic recrystallization behavior and properties of extruded Mg−9.5Gd−4Y−2.2Zn−0.5Zr (wt.%) alloy. The results showed that the volume fraction of fine grains was 17.4% for under-aged extruded (UAE) sample, while that of the peak-aged extruded (PAE) and over-aged extruded (OAE) samples reached 89.7% and 50.4%, respectively. Dense and fine β particles distributed inside grains and at grain boundaries significantly improved the nucleation sites and dislocation density through the particle-stimulated nucleation mechanism. However, the dense needle-like γ' phase inhibited dislocation slip and delayed dynamic recrystallization (DRX) nucleation. The difference in the fine grains between the PEA and OAE samples was attributed to a difference in the quantity and size of the original particles, and the difference in their tensile properties was caused by different microstructural components. The higher contributions of grain boundary strengthening and precipitation strengthening mechanisms gave PAE sample better tensile properties.

Key words: Mg−Gd−Y−Zn−Zr alloy; pre-ageing treatment; recrystallization behavior; strengthening mechanism; particle-stimulated nucleation

1 Introduction

With the rapid development of the aerospace and automotive industries, Mg−Gd−Y−Zn−Zr alloys, which are the most promising materials for main load-bearing components, have received extensive attention due to their low densities and excellent specific strengths [1−3]. However, low strength and poor formability caused by the insufficient slip system of the hexagonal close-packed (HCP) structure limit the wide application of magnesium (Mg) alloys [4−7]. Many researchers have proposed different methods for improving the strength and formability of Mg−Gd−Y−Zn−Zr alloys before forging them into complex components, and these enable Mg alloys to meet various complex requirements [8−10].

It is effective to promote grain refinement through thermomechanical processes and improve the properties of Mg alloys [11−13]. The severe plastic deformation (SPD) process can be repeated for multiple passes to increase the accumulated strain, refine grains and improve mechanical properties. Actually, the high equipment requirements and low-efficiency operation of the SPD process make it difficult to apply in production [14]. On the other hand, it is difficult to provide enough energy to promote grain refinement by traditional extrusion deformation during the preparation of large-size

Corresponding author: Yong XUE, Tel: +86-18536687936, E-mail: yongxue395@163.com;
Zhao-ming YAN, Tel: +86-15103468697, E-mail: zmyan1027@nuc.edu.cn
DOI: 10.1016/S1003-6326(23)66412-X

components, which is attributed to the limitations of material specifications and deformation degree. Therefore, researchers must develop a cost-effective and simple-to-operate process to solve these problems for industrial production of Mg alloys.

Researchers have recently reported that the particle introduced by pre-ageing treatment can significantly promote grain refinement of traditional AZ series alloys through the particle-stimulated nucleation (PSN) mechanism [15−19], thereby improving mechanical properties. In our previous research, we adopted the pre-peak-ageing process before extrusion of Mg−9.5Gd−4Y−2.2Zn−0.5Zr (wt.%) alloy, and found that the pre-existing Mg_5RE particles at the grain boundaries and within the grains aggravated the DRX behavior, which significantly improved strength [20]. This implies that a simple process involving pre-ageing treatment combined with traditional extrusion deformation to prepare a high-strength Mg−Gd−Y−Zn−Zr alloy may have prospects for industrial application. Interestingly, compared with the monotonous promotion of grain refinement by the precipitate ($Mg_{17}Al_{12}$) in the AZ series alloys, the various precipitates and complex ageing precipitation sequences in Mg−RE−Zn alloys may make it more difficult to explore the effects of pre-ageing treatment on microstructure and mechanical properties [9,21]. YU et al [22] proved that the pre-ageing treatment (410−470 ℃) significantly reduced the average grain size of extruded Mg−Gd−Y−Nd−Zn−Zr alloy because the resulting plate-like Mg_5RE precipitates promoted formation of high-angle grain boundaries. In contrast, WANG et al [23] reported that the DRX behavior of a pre-aged (200 ℃) Mg−Gd−Y−Zn−Mn alloy was significantly suppressed during the extrusion process, which was attributed to the hindering effects of metastable β' and γ' phases. These results indicated that different effects of pre-ageing treatment on the microstructure and mechanical properties of the deformed Mg-RE-Zn alloy can be attributed to deviations in ageing parameters (temperature or time) or alloy composition. Furthermore, it is worth noting that morphology and type of the ageing precipitates in the Mg−Gd−Y−Zn−Zr alloys gradually transformed with the prolonging of ageing time [24]. The whole ageing process can be divided into three states according to the corresponding ageing precipitation sequence and precipitation behavior: under-aged state, peak-aged state, and over-aged state [25]. At present, relevant research on the combination of pre-ageing treatment and deformation of Mg−Gd−Y−Zn−Zr alloy is mainly focused on the effects of pre-peak-ageing treatment on microstructure and properties [20,26]. The influence of different pre-ageing states on the microstructure and mechanical properties of the extruded Mg−Gd−Y−Zn−Zr alloy and the DRX mechanism of Mg−Gd−Y−Zn−Zr alloy in different pre-ageing states during extrusion are still unclear. Therefore, we investigated the effects of different pre-ageing states on the deformation behavior and mechanical properties of Mg−Gd−Y−Zn−Zr alloy to explore the possibility of pre-ageing treatment before extrusion to further expand the application scenarios for Mg−Gd−Y−Zn−Zr alloy.

In this work, the effects of three different pre-ageing states (under-aged state, peak-aged state, and over-aged state) on the microstructural evolution and mechanical properties of extruded Mg−9.5Gd−4Y−2.2Zn−0.5Zr (wt.%) alloy were studied. Moreover, the effects of different pre-ageing states on DRX behavior and the contribution of the dominant strengthening mechanism of extruded samples with different microstructures were discussed in detail.

2 Experimental

Mg−9.5Gd−4Y−2.2Zn−0.5Zr (wt.%) (determined by inductively coupled plasma-atomic emission spectrometry, ICP-AES) alloy ingot with dimensions of *d*420 mm × 660 mm was prepared by semi-continuous casting process. The *d*420 mm × 660 mm ingot was machined into multiple as-cast samples with the same specifications (*d*60 mm × 50 mm). Subsequently, all as-cast samples were solution-treated at 520 °C for 24 h, and quenched in cold water to accelerate the cooling rate. To prepare samples with different ageing states, three different times were selected for solution-treated samples aged at 200 °C based on previous research [9]. Solution-treated samples aged at 200 °C for 64 h were defined as under-aged samples (UA samples), solution-treated samples aged at 200 °C for 112 h were defined as peak-aged samples (PA samples), and solution-treated samples aged at 200 °C for 256 h were defined as over-aged samples (OA

samples). Solution treatment and ageing treatment samples were pre-heated at 450 °C for 40 min before extrusion to ensure uniform temperature. Moreover, the extrusion die was held at 450 °C for 5 h. After pre-heating treatment, the samples were deformed by hot extrusion with an extrusion ratio of 16:1, and finally the extruded samples with a diameter of 15 mm were prepared. The solution-treated samples after extrusion were defined as the SE sample. The UA samples after extrusion were defined as UAE samples. The PA samples after extrusion deformation were defined as PAE samples. The OA samples after extrusion were defined as OAE samples. In addition, solution-treated samples with diameters of 70 mm were subjected to extrusion deformation with an extrusion ratio of 22:1 under the same conditions to compare the grain refinement effect of the pre-ageing treatment, and these were defined as SE70 samples. Detailed heat treatment parameters are listed in Table 1.

Table 1 Heat treatment parameters of different samples and corresponding abbreviations

Designation	Thermal condition
Solution treatment	520 ℃, 24 h
UA	(520 ℃, 24 h) + (200 ℃, 64 h)
PA	(520 ℃, 24 h) + (200 ℃, 112 h)
OA	(520 ℃, 24 h) + (200 ℃, 256 h)
SE	Solution treatment + extrusion (16:1, 450 ℃)
SE70	Solution treatment + extrusion (22:1, 450 ℃)
UAE	UA + extrusion (16:1, 450 ℃)
PAE	PA + extrusion (16:1, 450 ℃)
OAE	OA + extrusion (16:1, 450 ℃)

All samples were mechanically ground and polished before microstructure observation with scanning electron microscopy (SEM, Hitachi SU5000). To understand the grain orientation, grain size distribution and texture, the samples were electrochemically polished in a perchloric acid−alcohol solution (volume ratio 1:9) at −30 °C before performing electron backscatter diffraction (EBSD) characterization. Subsequently, TSL-OIM software (version 7.3) was used to further process and analyze of the EBSD data (for example, misorientation angle and local dislocation distribution). The nanoscale microstructures of different extruded samples were investigated by transmission electron microscopy (TEM, JEOL JEM-F200). Thin foil samples were prepared by ion beam thinner (Leica Em Res102) for TEM observation. The volume fraction and diameter of the particle phase of different samples were measured from low magnification TEM brightfield images using Image-Pro Plus 6.0 software, and each sample was measured at least 5 times [27,28].

Room temperature (RT, 25 °C) tensile properties of all samples were determined with a uniaxial tensile testing machine (Instron−3382). Tensile specimens with a thickness of 2 mm, a gauge length of 25 mm and a gauge length of 6 mm were processed by electric discharge cutting. The tensile test with an engineering strain rate of 0.001 s^{-1} was repeated three times under the same conditions to ensure the accuracy of the results.

3 Results

3.1 SEM and EBSD images of different samples before extrusion deformation

Figure 1 shows SEM images of samples after different heat treatments. The microstructures of different pre-aged samples were different after pre-heating treatment, except that bulk lamellar long period stacking ordered (LPSO) phase was distributed at the grain boundaries of all samples (marked by red arrows in Fig. 1). Interestingly, the modifications from the UA samples before and after pre-heating treatment were indistinguishable from the SEM images. Therefore, it is necessary to observe its higher magnification images by TEM. Obviously, needle γ' phase (marked by blue arrows in Figs. 1(b) and (c)) and β'' phase (marked by green arrows in Figs. 1(b) and (c)) were distributed in the UA sample, as indicated by the corresponding TEM image and SAED pattern. After pre-heating treatment, the β'' phase in the UA sample disappeared, and the γ' phase remained (Figs. 1(d–f)). Compared with the UA sample, the lamellar LPSO phase (marked by purple arrows in Fig. 1) and many particles were distributed at the grain boundaries or inside the grains (marked by yellow ellipses and arrows in Figs. 1(g–j)) of the PA and OA samples, and these particles have been proven

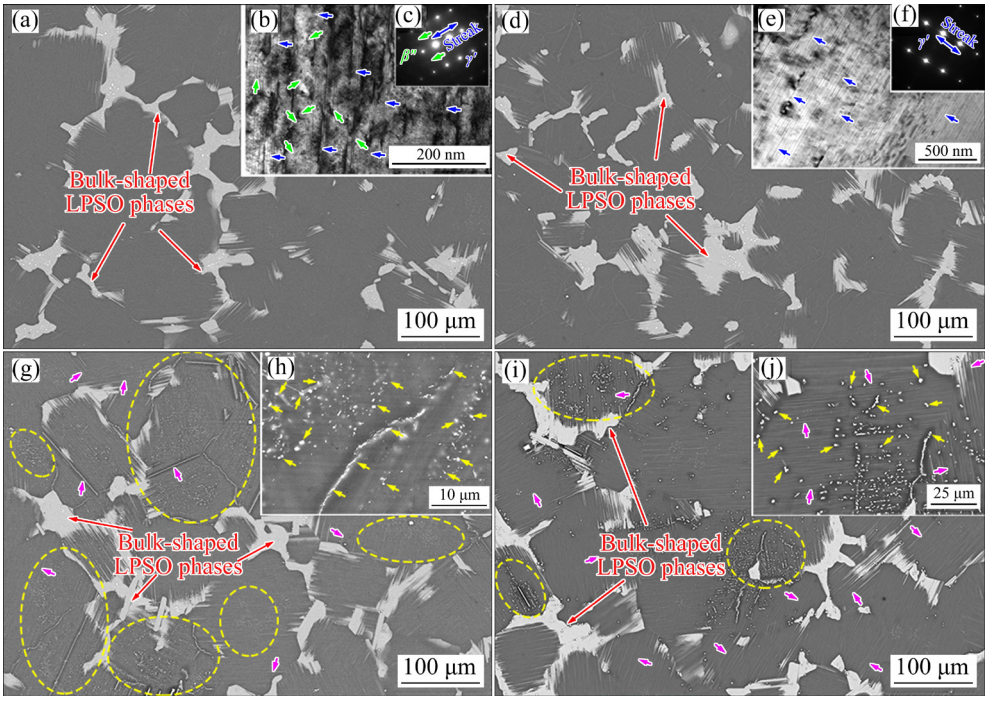

Fig. 1 SEM images (a, d, g−j), TEM bright field images (b, e) and SAED patterns (c, f) of different samples after heat treatment at 450 °C for 40 min: (a−c) UA sample; (d−f) UA sample; (g, h) PA sample; (i, j) OA sample

to be Mg_5RE phase that transformed from β' phase [20]. In addition, it can be seen that the PA sample has denser and finer particles by comparing the microstructures of the OA sample (Figs. 1(i) and (j)) and the PA sample (Figs. 1(g) and (h)) after pre-heating treatment. The difference in the type and quantity of the second phase of the pre-aged samples after pre-heating may be related to ageing precipitation behavior of the Mg−Gd−Y−Zn−Zr alloy.

3.2 SEM and EBSD images of different samples after extrusion deformation

To facilitate understanding, a schematic illustration of the microstructure observation positions of the extruded samples is shown in Fig. 2(a). Figures 2(b−f) show the microstructures of different samples after extrusion (−10 mm). The grains with grain orientation spread (GOS) < 2 are defined as fine recrystallized grains [29]. The bulk LPSO phase appears black in the IPF maps because it cannot be indexed. The low-angle grain boundaries (LAGBs, with misorientation angles between 2° and 15°) are marked with white lines and the high-angle grain boundaries (HAGBs, with misorientation angles greater than 15°) are marked with black lines. Most samples have typical bimodal microstructures with coarse deformed grains surrounded by fine recrystallized grains, which indicates insufficient recrystallization. The average grain size and volume fraction of fine grains in the SE sample were 2.7 μm and 36.1%, respectively. As the cumulative strain increased (extrusion ratio: 16∶1→22∶1), the volume fraction of fine grains of the SE70 sample also increased (47.6%). This indicates that increasing the extrusion ratio provides more energy for the formation of fine grains, thereby promoting activation of the recrystallization mechanism [30]. In contrast, the average grain size and volume fraction of fine grains in pre-aged samples showed different evolution laws. The average grain size and volume fraction of fine grains in the UAE sample were significantly reduced, and were 1.9 μm and 17.4%, respectively. Interestingly, the volume fraction of fine grains in the PAE sample and the OAE sample increased significantly, even exceeding that of the SE70 sample. The average grain size and volume fraction of fine grains in the OAE sample were 2.3 μm and 50.4%, respectively. The volume fraction of fine grains in the PAE sample was 89.7%, which is the highest among all samples.

In general, the above results indicated that compared with traditional solution extrusion,

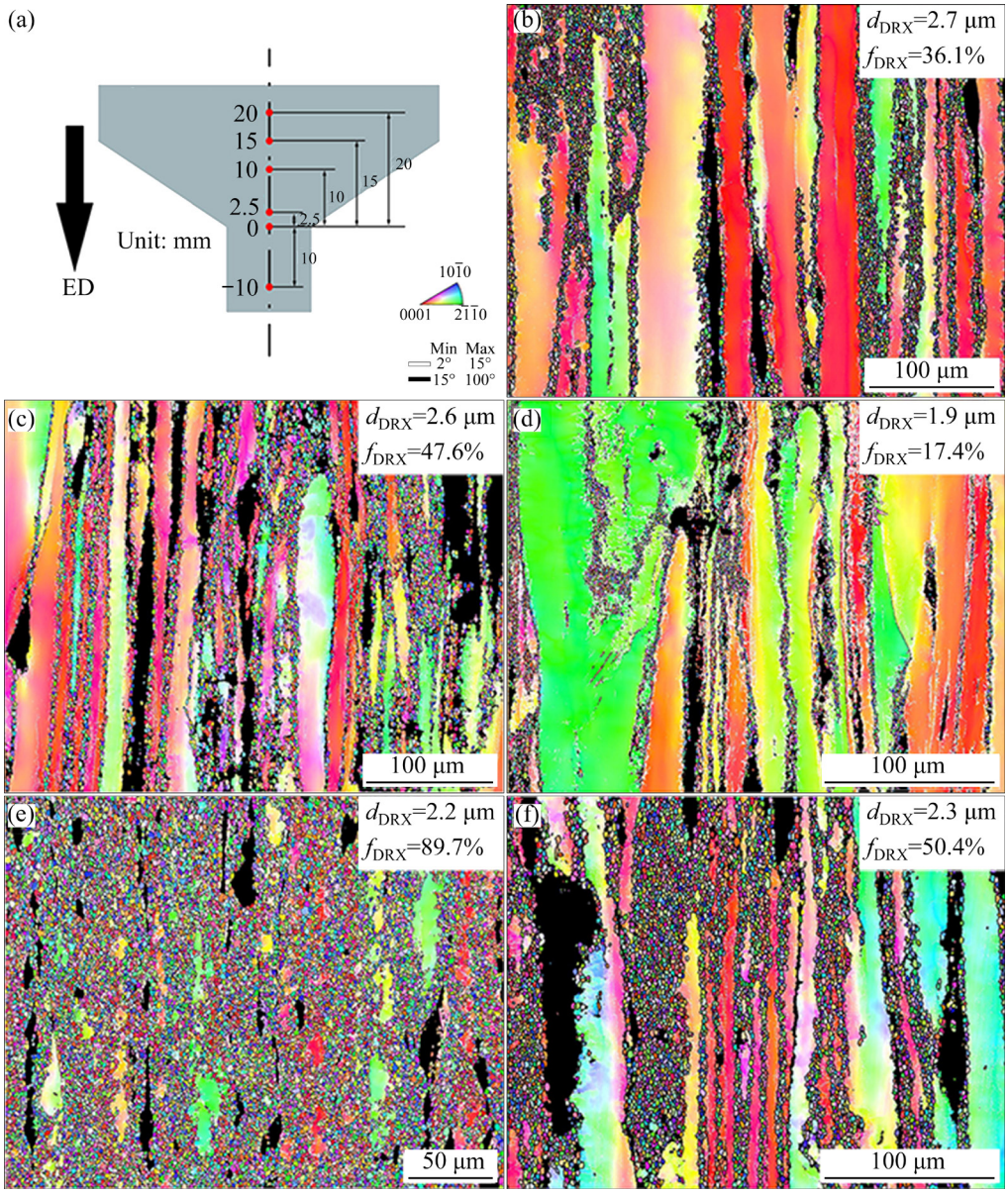

Fig. 2 Microstructure observation locations for extruded sample (a) and EBSD IPF maps (b−f) of different samples after extrusion (−10 mm): (b) SE sample; (c) SE70 sample; (d) UAE sample; (e) PAE sample; (f) OAE sample

pre-ageing treatment before extrusion can be used to tailor the microstructure with different pre-ageing time: UA treatment inhibits grain refinement, while PA or OA treatment has the opposite effect. The significant difference in the volume fractions of fine grains among the pre-aged samples was attributed to their initial microstructures. Therefore, to deeply understand the deformation behavior of the pre-aged samples during extrusion, we selected two samples with typical characteristics: the UAE sample (the lowest volume fraction of fine grains) and the PAE sample (the highest volume fraction of fine grains). The recrystallization behavior of these two samples at different extrusion stages will be discussed below.

The microstructure of the UAE sample at the initial extrusion stage (20 mm above the mold exit) is shown in Fig. 3. Obviously, the IPF map (Fig. 3(a)) and the corresponding boundary misorientation map (Fig. 3(e)) indicate that many $\{10\bar{1}2\}$ tensile twins were activated. On the other hand, the misorientation angles were less than 4° in the non-twinned original grains from the corresponding line profiles of the misorientation angle along the black arrows AB (Fig. 3(f)) and CD (Fig. 3(g)), which reveals the low dislocation density in the non-twinned original grains. These results indicate that $\{10\bar{1}2\}$ tensile twinning is

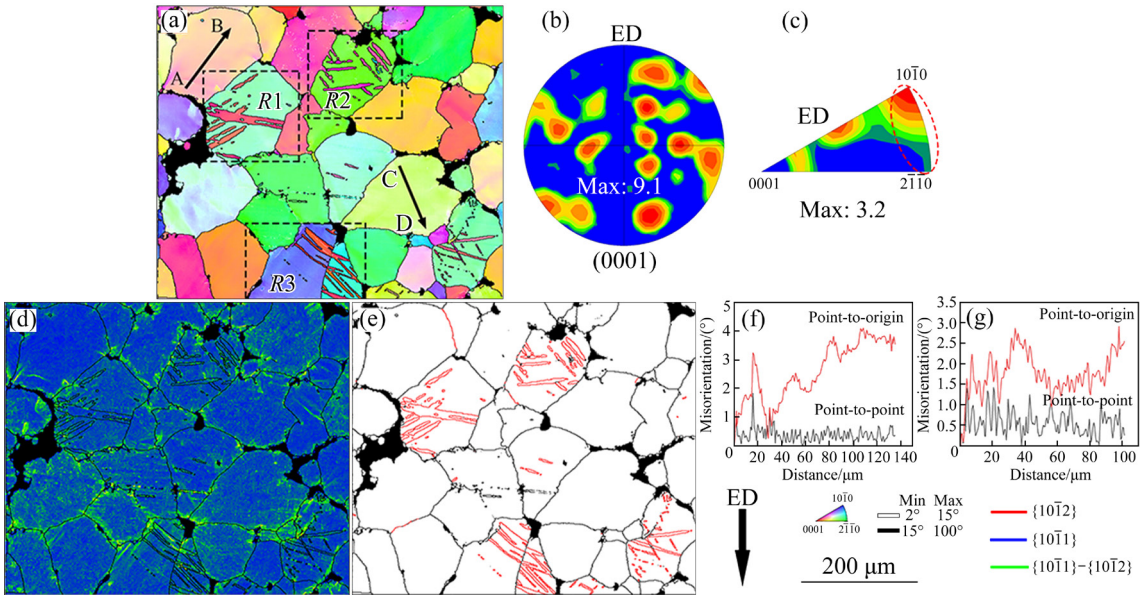

Fig. 3 EBSD results of UAE sample at 20 mm above mold exit: (a) EBSD IPF map; (b) (0001) pole figure; (c) Inverse pole figure; (d) Corresponding KAM map; (e) Corresponding boundary misorientation map; (f) Line profiles of misorientation angle along black arrow AB in (a); (g) Line profiles of misorientation angle along black arrow CD in (a)

the dominant deformation mechanism for UAE samples at the initial extrusion stage (20 mm). In addition, the (0001) basal planes of the UAE sample have relatively random orientations (Fig. 3(b)), while the corresponding inverse pole figure illustrates the appearance of the $[10\bar{1}0]$–$[2\bar{1}\bar{1}0]$ component (marked by the red dashed ellipses in Fig. 3(c)). Furthermore, several typical regions were selected to further observe the orientation relationship between $\{10\bar{1}2\}$ twins and parent grains and the effect of $\{10\bar{1}2\}$ twins on the texture. Figure 4 shows EBSD results of different regions of interest selected from Fig. 3(a) (*R*1, *R*2 and *R*3). Activation of various $\{10\bar{1}2\}$ twin variants not only consumed the parent grains but also changed the orientation: from the *c*-axis//ED (orientation of the parent grains) to the *c*-axis⊥ED (orientation of the $\{10\bar{1}2\}$ twin) (Figs. 4(a, e, i)). This is consistent with the observed for the (0001) pole figures: the (0001) basal texture of the parent grains was deflected from the ED polar zone to the equatorial zone (86°±5°). Moreover, the corresponding inverse pole figures showed that the formation of the $[10\bar{1}0]$–$[10\bar{1}2]$ component was mainly attributed to the reorientation of various twin variants (Figs. 4(d, h, l)). These observations indicate that the deformation behavior and grain reorientation of the UAE samples were closely related to the $\{10\bar{1}2\}$ tensile twins at the initial extrusion stage (20 mm).

Figure 5 shows the EBSD results of PAE samples at the initial extrusion stage (20 mm). The kernel average misorientation (KAM) can reflect local strain or dislocation density distribution within the grains. Many LAGBs were located inside the original grains, except for a few $\{10\bar{1}2\}$ tensile twins that were activated. According to the corresponding KAM maps and SEM images, regions with higher KAM values almost corresponded to regions where the particles were distributed, not only along the grain boundaries but also inside the grains (marked by the red arrows in Figs. 5(d, e). Similarly, the PEA sample also had a $[10\bar{1}0]$–$[2\bar{1}\bar{1}0]$ component, but the pole intensity of the (0001) basal texture (8.7) was slightly reduced compared with that of the UAE sample (9.1). Therefore, to further understand the deformation behavior of the PEA sample at the initial extrusion stage (20 mm), regions of interest in Fig. 5(a) were selected for further analysis.

Figure 6 shows the EBSD results of the *R*1 and *R*2 regions selected from Fig. 5(a). The EBSD observation results of the *R*1 region showed that three different lenticular $\{10\bar{1}2\}$ twin variants were activated, which led to consumption and reorientation of the parent grains, thereby forming a typical $[10\bar{1}0]$–$[11\bar{2}0]$ composition (Figs. 6(a−d)). This confirmed that the effects of $\{10\bar{1}2\}$ twins

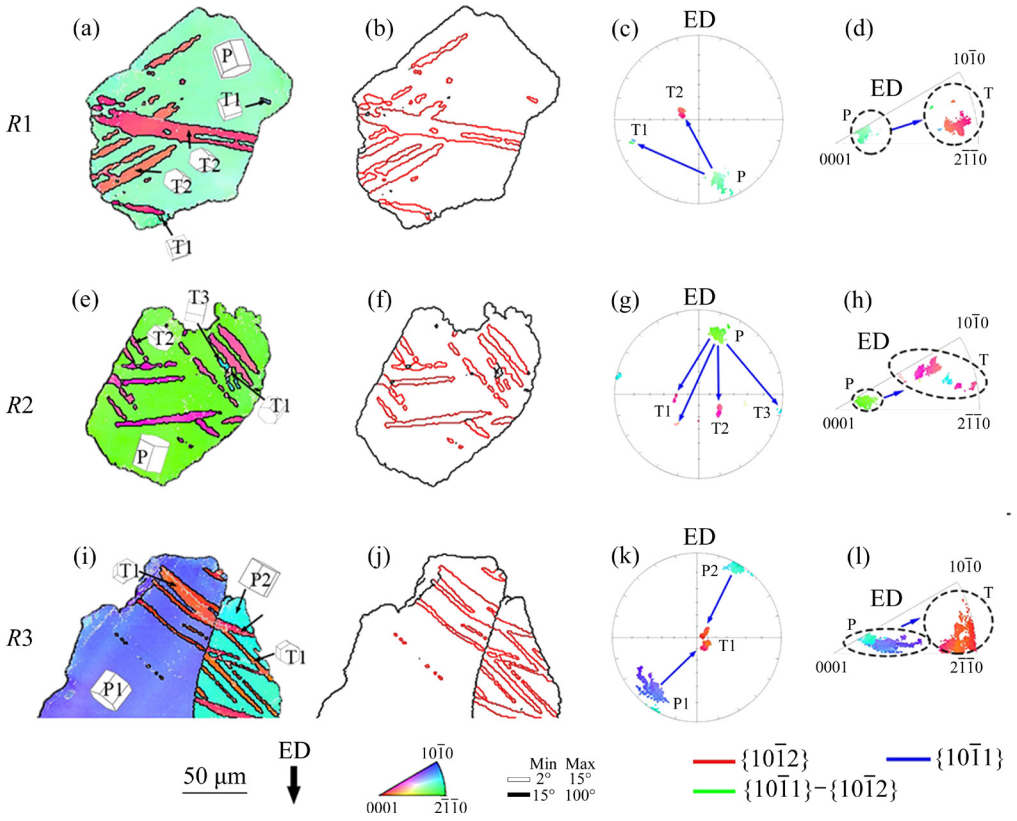

Fig. 4 EBSD results of different regions selected from Fig. 3(a): (a−d) *R*1; (e−h) *R*2; (i−l) *R*3; (a, e, i) EBSD IPF maps; (b, f, j) Corresponding boundary misorientation maps; (c, g, k) (0001) pole figures; (d, h, l) Inverse pole figures

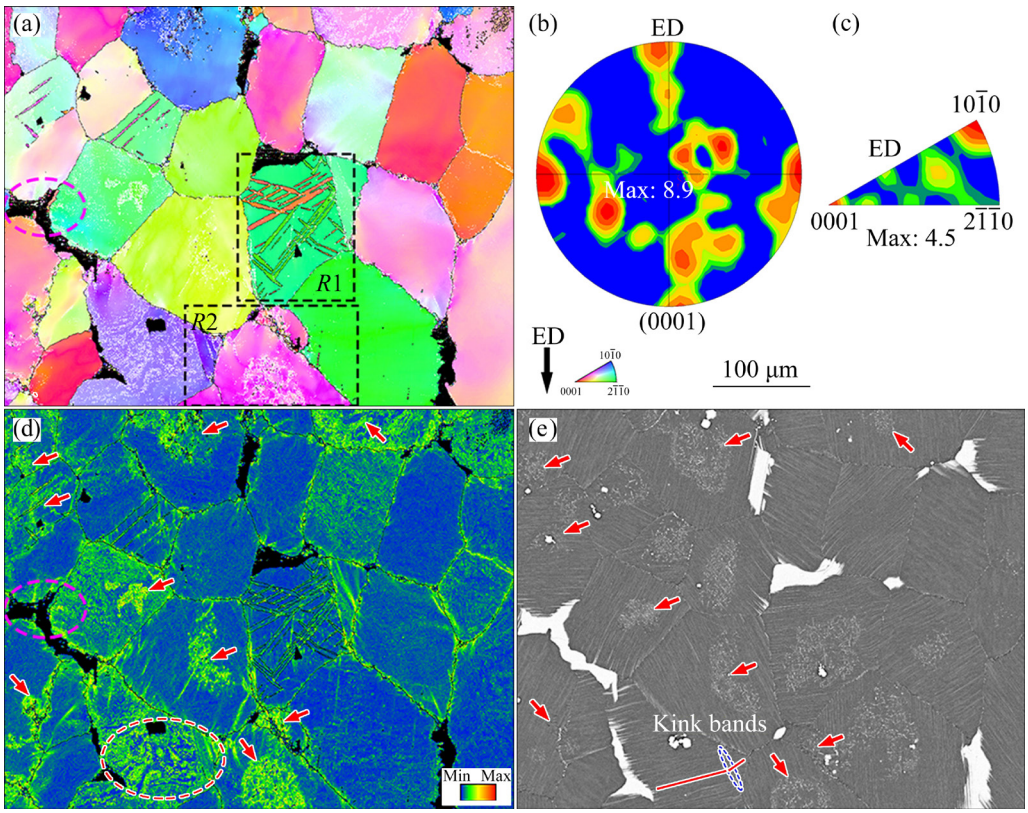

Fig. 5 EBSD results of PAE sample at 20 mm above mold exit: (a) EBSD IPF map; (b) (0001) pole figure; (c) Inverse pole figure; (d) Corresponding KAM map; (e) Corresponding SEM image

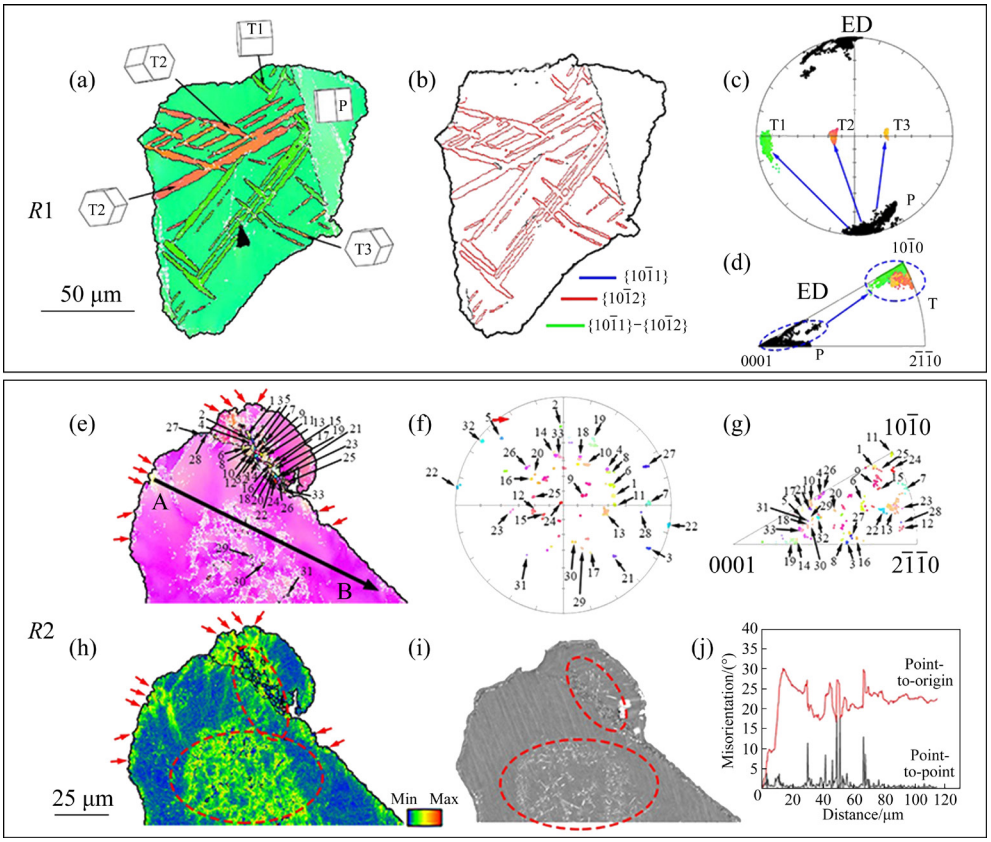

Fig. 6 EBSD results of different regions selected from Fig. 5(a): (a−d) *R*1; (e−j) *R*2; (a, e) EBSD IPF maps; (b) Boundary misorientation map corresponding to (a); (c, f) (0001) pole figures; (d, g) Inverse pole figures; (h) KAM map corresponding to (e); (i) SEM image corresponding to (e); (j) Line profiles of misorientation angle along black arrow AB in (e)

in PAE samples and UAE samples were consistent, although the number of twins in the former was much lower than that in the latter. In contrast, in the *R*2 region, many fine grains were distributed around the particles inside the original grains, as well as sub-grain clusters and LAGBs (marked by the red dashed ellipses in Figs. 6(e, h, i), which differs significantly different from the UAE sample (Fig. 3). PENG et al [31] and KANG et al [32] also reported that the original particles can aggravate the DRX nucleation process through the PSN mechanism. These results indicate that the PSN mechanism as the dominant deformation mechanism, accelerated the accumulation of strain through the interaction of particles and dislocations, thereby promoting the formation of high-density dislocations and fine grains of the PAE sample at the initial extrusion stage (20 mm). Furthermore, Figs. 6(f) and (g) show that the fine grains have random orientations, which may cause the pole intensity of the (0001) basal texture of the PAE sample to decrease. The line profile of the point-to-origin along arrow AB (Fig. 6(e)) shows that the misorientation angle exceeded 20°, and the jagged grain boundaries (marked by the red arrows in Figs. 6(e) and (h)) indicated that the continuous dynamic recrystallization (CDRX) and discontinuous dynamic recrystallization (DDRX) mechanisms were activated in the PAE sample at the initial extrusion stage (20 mm). The abovementioned EBSD observation results for UAE and PAE samples at the initial extrusion stage (20 mm) revealed that the original microstructures significantly affected subsequent deformation behavior and microstructure evolution.

Figure 7 shows the EBSD results of the UAE sample after further deformation (15 mm). The results showed that the grain boundaries of the original grains gradually bulged toward the adjacent grains and finally formed the isolated fine grains (marked by the black arrows in Fig. 7(a)), which is a typical DDRX mechanism. On the other hand, the

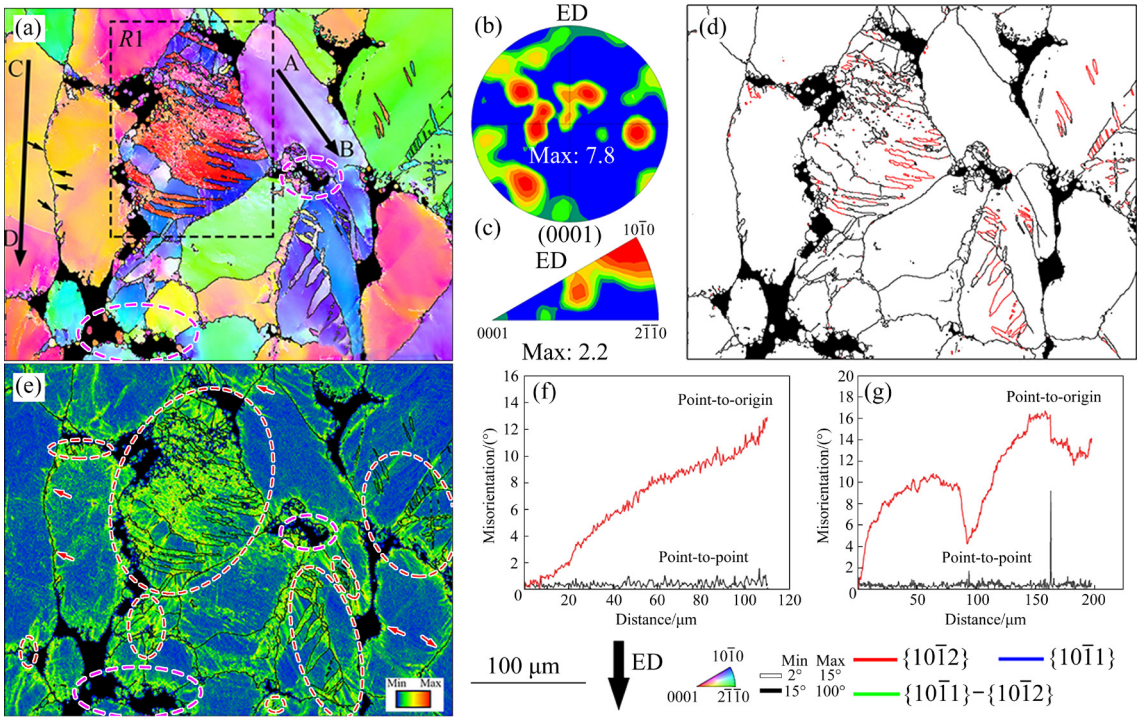

Fig. 7 EBSD results of UAE sample at 15 mm above mold exit: (a) EBSD IPF map; (b) (0001) pole figure; (c) Inverse pole figure; (d) Corresponding boundary misorientation map; (e) Corresponding KAM map; (f) Line profiles of misorientation angle along black arrow AB in (a); (g) Line profiles of misorientation angle along black arrow CD in (a)

line profiles along arrows AB and CD show that the misorientation angle gradually rose to 13° (Figs. 7(f) and (g)), indicating that the orientation of the original grains underwent a continuous change due to accumulated dislocations, that is, the CDRX mechanism. These results prove that the movement dislocations in the original grains of the UAE samples increased with further deformation, which gradually activated the CDRX and DDRX mechanisms. Interestingly, the higher density of dislocations segregated in the $\{10\bar{1}2\}$ twin regions (marked by red ellipses in Fig. 7(e)) compared with the non-twinned original grains (marked by the red arrows in Fig. 7(e)) according to the corresponding boundary misorientation map and KAM map.

Therefore, the EBSD results for the region *R*1 selected from Fig. 7(a) are illustrated in Fig. 8, to explore the deformation behavior of $\{10\bar{1}2\}$ twins at this extrusion stage (15 mm). It was clear that the parent grain area was mainly composed of blue and purple colors, while the twin area was red (Fig. 8(a)). Compared with the extrusion deformation of the UAE sample at the 20 mm stage (Figs. 3 and 4), the twin boundaries expanded and gradually depleted the parent grains with further deformation. The observation results of the line profiles along arrows AB and CD located in the twins and the parent grains are consistent with the corresponding KAM map (Fig. 7(e)), and the point-to-origin misorientation angles (~30°) were significantly higher than those of the non-twinned original grains (~14°), which should be attributed to the fact that reorientation is more prone to dislocation activation. CUI et al [33] confirmed that twin boundaries can also serve as nucleation sites to promote the formation of fine grains. Therefore, the high-density dislocations that are prone to segregate in the twin regions contribute to the formation of fine grains with random orientation, which is a typical TDRX mechanism. The above microstructure results clearly revealed that the deformation behavior of $\{10\bar{1}2\}$ twins (TDRX) was still dominant with gradual activation of the CDRX and DDRX mechanisms in the UAE sample upon further extrusion deformation (15 mm).

The EBSD results for the PAE sample at 15 mm above the mold exit are presented in Fig. 9. Denser fine grains were distributed inside the original grains and along the grain boundaries of the

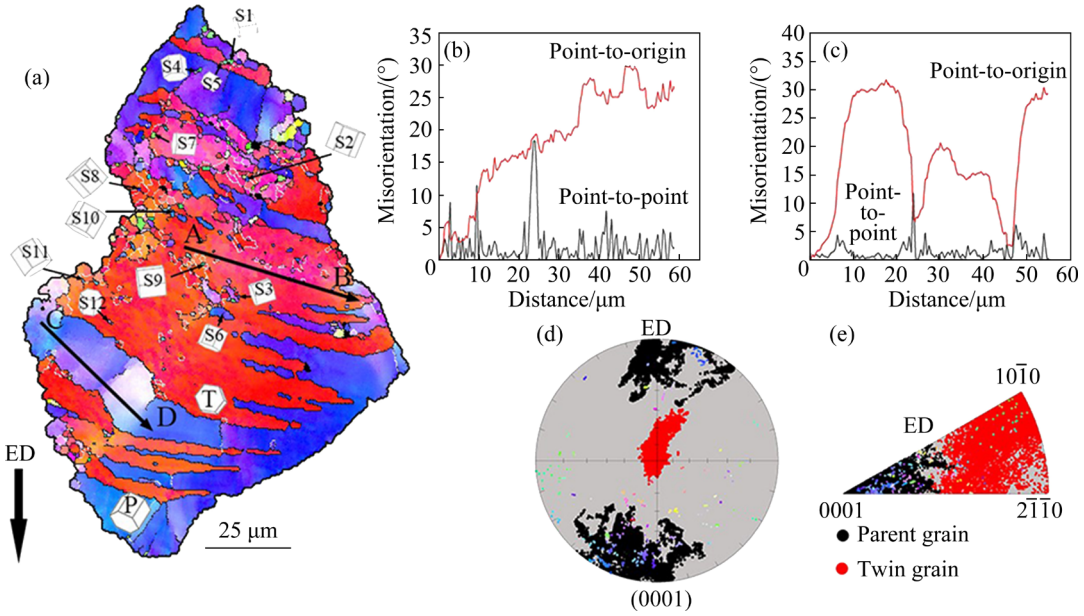

Fig. 8 EBSD results of *R*1 region selected from Fig. 7(a): (a) EBSD IPF map; (b) Line profiles of misorientation angle along black arrow AB in (a); (c) Line profiles of misorientation angle along black arrow CD in (a); (d) (0001) pole figure; (e) Inverse pole figure

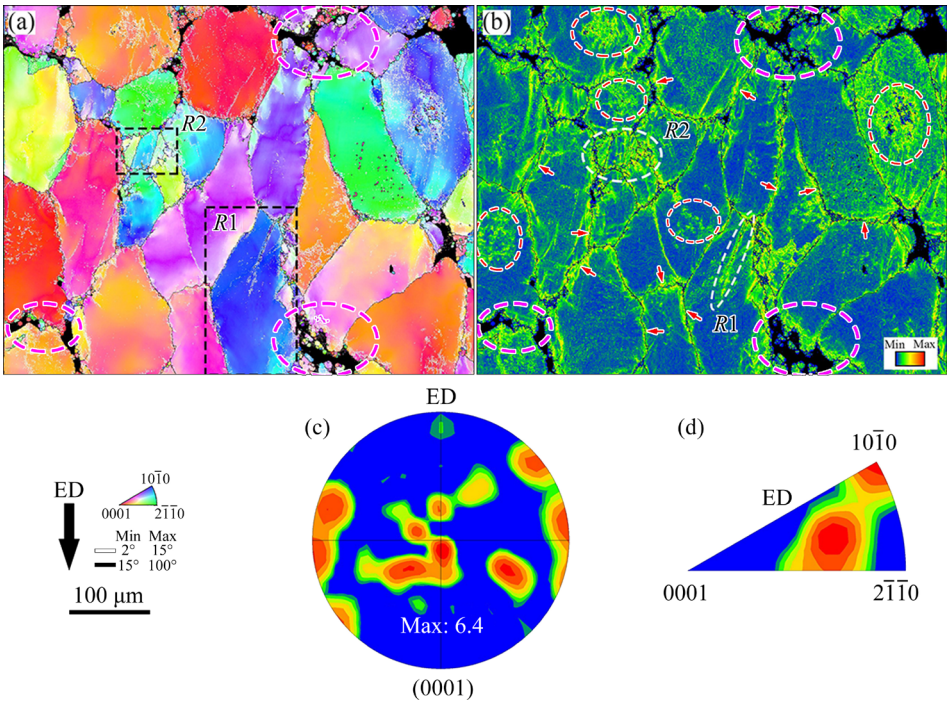

Fig. 9 EBSD results of PAE sample at 15 mm above mold exit: (a) EBSD IPF map; (b) Corresponding KAM map; (c) (0001) pole figure; (d) Inverse pole figure

PAE sample (Fig. 9(a)), which indicated that more driving energy was provided from further deformation to promote the activation of the recrystallization mechanisms (PSN, CDRX and DDRX mechanisms). High-density dislocations (regardless of grain boundaries or intragranular) were still mostly distributed around the particle regions according to the corresponding IPF and KAM maps (marked by the red arrows and ellipses in Fig. 9(b)), which indicated that the PSN mechanism still made the dominant contribution to the grain refinement at the further extrusion stage (15 mm). Unexpectedly, many dislocations accumulated inside the particle-free original grains

(marked by the white ellipses in Fig. 9(b)). Therefore, two different regions were selected to observe the deformation characteristics of these grains. The EBSD results and SEM images of different regions selected from Fig. 9(a) are shown in Fig. 10.

Obviously, the chain structure (marked by the yellow arrows in Fig. 10(a)) was formed at the original grain boundaries and gradually extended along the LAGBs into the parent grain in the *R*1 region (marked by the red arrows in Fig. 10(a)). The SEM image corresponding to the chain structure indicated that the kink bands of the lamellar LPSO phase were broken and fine particles were precipitated (marked by the blue ellipses in Fig. 10(b)). Moreover, the LAGB clusters surrounding the chain structure (Fig. 10(a)) indicated that high-density dislocations were distributed around the kink bands and extended along the kink bands into the parent grains (marked by the red arrows in Fig. 10(a)). MENG et al [34] proved that high-density dislocations gathered at the kink bands of the lamellar LPSO phase tended to form HAGBs, thereby promoting grain refinement.

The EBSD results and SEM images of the *R*2 region further proved that the grain boundaries of the new grains gradually penetrated the parent grains along the kink bands, which were isolated from the parent grains. The corresponding (0001) pole figures (Figs. 10(c) and (g)) show that the new grains formed in the kinked region were reoriented compared to the parent grains, and the deflection angle of the *c*-axis is consistent with the kinking angle [35]. In addition, the newly formed grains have a typical abnormal texture (*c*-axis//ED) according to the inverse pole figures (Figs. 10(d) and (h)) of the two regions (*R*1 and *R*2), which may provide a new way to explain the mechanism for the formation of abnormal texture [30,36,37]. Therefore, the significant decrease in texture strength of the PEA sample (0001) from 8.9 (Fig. 5(b)) to 6.4 (Fig. 9(c)) can be attributed to the formation of more fine grains with random orientation and new grains induced by kink bands with abnormal texture.

In general, with further deformation, grain refinement of the PEA sample was promoted by

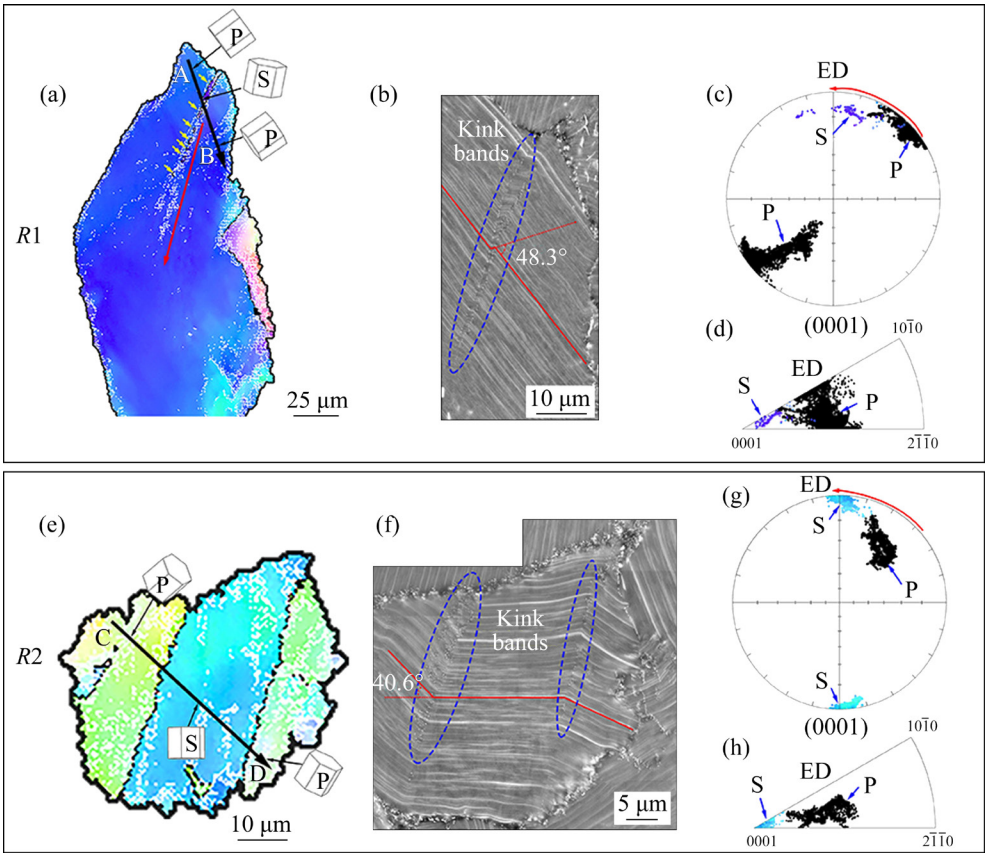

Fig. 10 EBSD results and SEM images of different regions selected from Fig. 9(a): (a−d) *R*1; (e−h) *R*2; (a, e) EBSD IPF maps; (b, f) Corresponding SEM images; (c, g) (0001) pole figures; (d, h) Inverse pole figures

aggravating the PSN, CDRX and DDRX mechanisms, and also by the formation of new grains induced by high-density dislocations at the kink bands, which also contributed to subdivision of the original grains. The above results indicate that there are significant differences in the activation of the recrystallization mechanism for different samples with various initial micro-structures. Apart from that, the hard-brittle bulk LPSO strengthening phase present in all samples played a similar role during deformation. In UAE and PAE samples, the high localized dislocations accumulated around the bulk LPSO phase induce the formation of fine recrystallized grains as the deformation degree increases (marked by the pink ellipses in Figs. 3−9). RAMEZANI et al [38] investigated the grain refinement mechanism of multi-directional forged (MDFed) GWZ Mg alloys and confirmed that the high-density dislocations near the bulk LPSO phase can provide the energy required for new grain formation. The main focus of this work is the effect of different initial microstructures on the subsequent recrystallization behavior, so the bulk LPSO phase common to all samples will be further discussed in depth in other studies.

Figure 11 shows microstructures of UAE and PAE samples at 10 mm above the mold exit. Fine grains of the UAE sample were basically distributed along the grain boundaries of the deformed grains, and the volume fraction of fine grains was only 6.1%. In contrast, the grain refinement of the PAE sample was significantly increased due to the higher dislocation density and abundant recrystallization behavior, and the volume fraction of fine grains reached 25.9%, which was more than four times that of the UAE sample. On the other hand, the distributions and quantities of the second phase between different samples were also inconsistent according to the corresponding SEM images. Compared with the particles of the UAE sample, which were mainly distributed along the grain boundaries of the deformed grains (marked by the yellow ellipses in Fig. 11(d)), the denser particles in the PEA sample were distributed along the grain boundaries and also in the deformed grains (marked by the yellow ellipses in Fig. 11(f)).

The grain refinement degree was significantly increased for all samples at the final extrusion stage. Figure 12 shows microstructures of UAE and PAE samples at 2.5 mm above the mold exit. The deformed grains in all samples were elongated along the ED. The microstructural compositions of UAE samples were still dominated by deformed

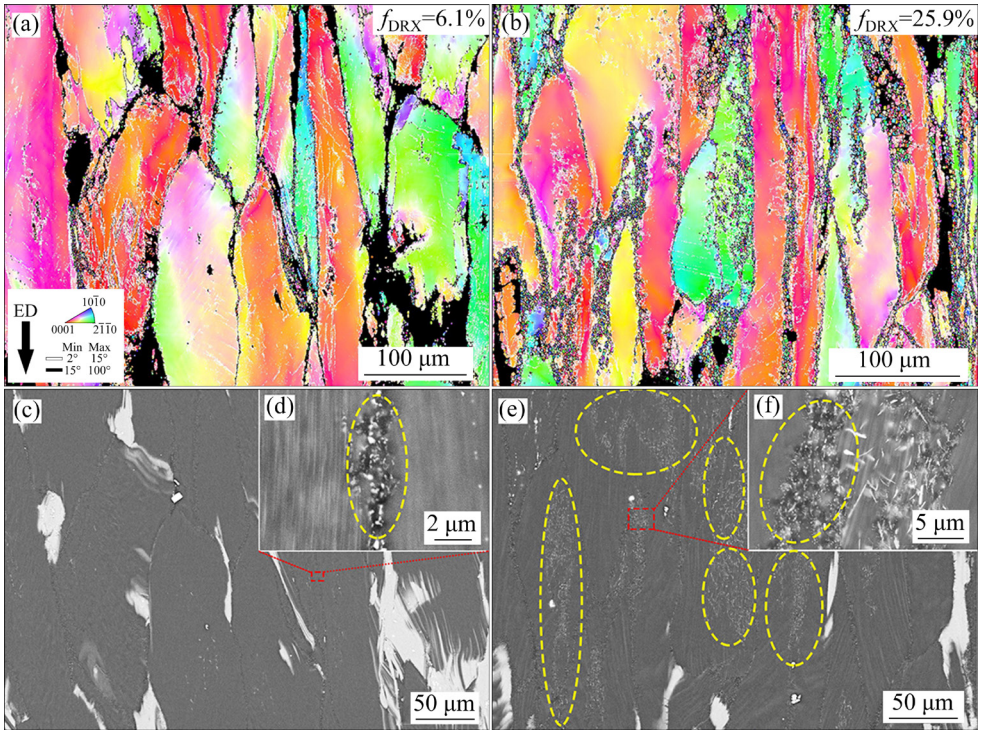

Fig. 11 Microstructures of different samples at 10 mm above mold exit: (a, c, d) UAE sample; (b, e f) PAE sample; (a, b) EBSD IPF maps; (c−f) Corresponding SEM images

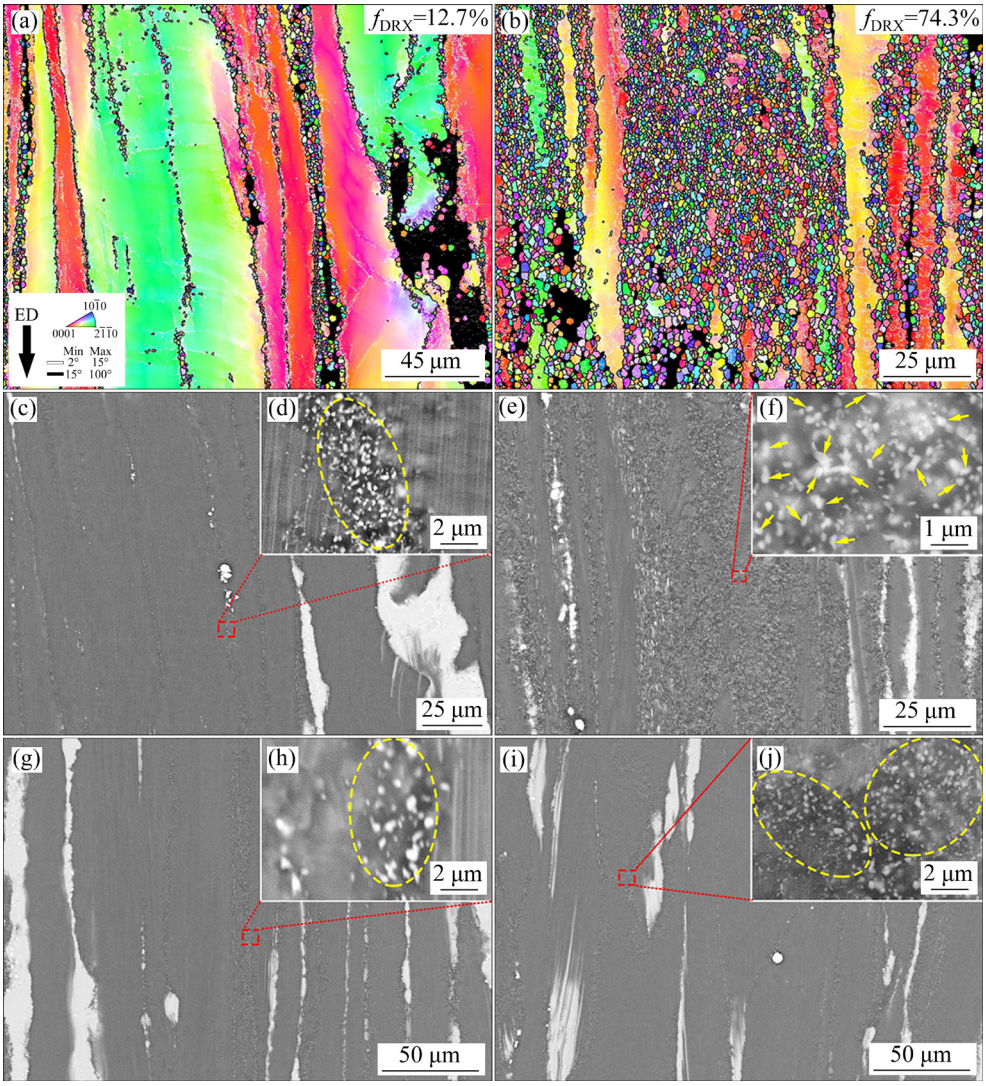

Fig. 12 Microstructures of different samples at 2.5 mm above mold exit: (a, c, d) UAE sample; (b, e f) PAE sample; (g, h) SE sample; (i, j) OAE sample; (a, b) EBSD IPF maps; (c−j) SEM images

grains, and the volume fraction of fine grains was only 12.7%. However, the volume fraction of the deformed grains in the PAE sample was significantly reduced, and most of its microstructure components were occupied by fine grains. The volume fraction of fine grains in the PAE sample was almost six times that of the UAE sample.

In addition, the SEM images of all samples are shown in Figs. 12(c−j). As indicated by high magnification SEM images of all samples, the fine particles of all samples were mainly distributed in the fine grain region, and the distribution of the particles of the PAE sample was the densest (marked by the yellow arrows in Fig. 12(f)). In contrast, the SE sample had the smallest proportion of Mg_5RE phase, which was limited by dynamic precipitation during the deformation process [20,39].

The above results indicate that UAE and PAE samples with different initial microstructures utilized different DRX mechanisms during extrusion. The recrystallization behaviors of UAE sample were dominated by the TDRX mechanism at the initial extrusion stage (20 mm), while the DDRX and CDRX mechanisms were activated as the degree of deformation increased (15 mm). However, the PSN, CDRX and DDRX mechanisms were the main recrystallization paths for PAE sample at the initial extrusion stage (20 mm), which significantly promoted the grain refinement. Moreover, with further extrusion (15 mm), interactions between dislocations and kinked bands of the lamellar LPSO phase also contributed to the grain refinement in the PEA sample.

3.3 TEM images of different samples after extrusion deformation

To further explore the distribution and quantity of particles, the microstructures of different samples were observed after extrusion by TEM. Figure 13 shows TEM bright-field images for different samples after extrusion. The fine grain regions of all samples were distributed with nanoparticles (marked by the yellow arrows in Fig. 13(d)), which was consistent with the SEM images in Figs. 12(c−j). However, there were significant differences in the quantities of nanoparticles in different samples. Obviously, the volume fraction of nanoparticles in the SE sample was the lowest, only 1.51%. The nanoparticles of pre-aged extruded samples (UAE, PAE and OAE) were denser than those of SE samples. The volume fraction of the nanoparticles in the UAE sample was 3.91%. By comparison, the extruded samples with longer pre-ageing times had more nanoparticles. The volume fraction of the nanoparticles in the OAE sample was 2.1 times that of the UAE sample, which reached 8.22%. However, the volume fraction of the nanoparticles did not monotonically increase with the pre-ageing time. The PAE sample had the highest volume fraction of nanoparticles among all samples (10.5%). On the other hand, the nanoparticles (marked by the yellow arrows in Fig. 13(d)) were distributed at the grain boundaries of the fine grain region (marked by the blue dotted line in Fig. 13(d)), which improved the strength of the grain boundaries with the pinning effect [40,41]. As a strengthening phase, the nanoparticle phase can improve the strength of the alloy by hindering the movement of dislocations (the mechanism of bypassing or cutting between the dislocation and the particles); moreover, particles located at the grain boundaries can also inhibit the migration of the grain boundaries through pinning effect and improve the ability of the grain boundaries to resist deformation (Fig. 13), which makes crack initiation and propagation difficult.

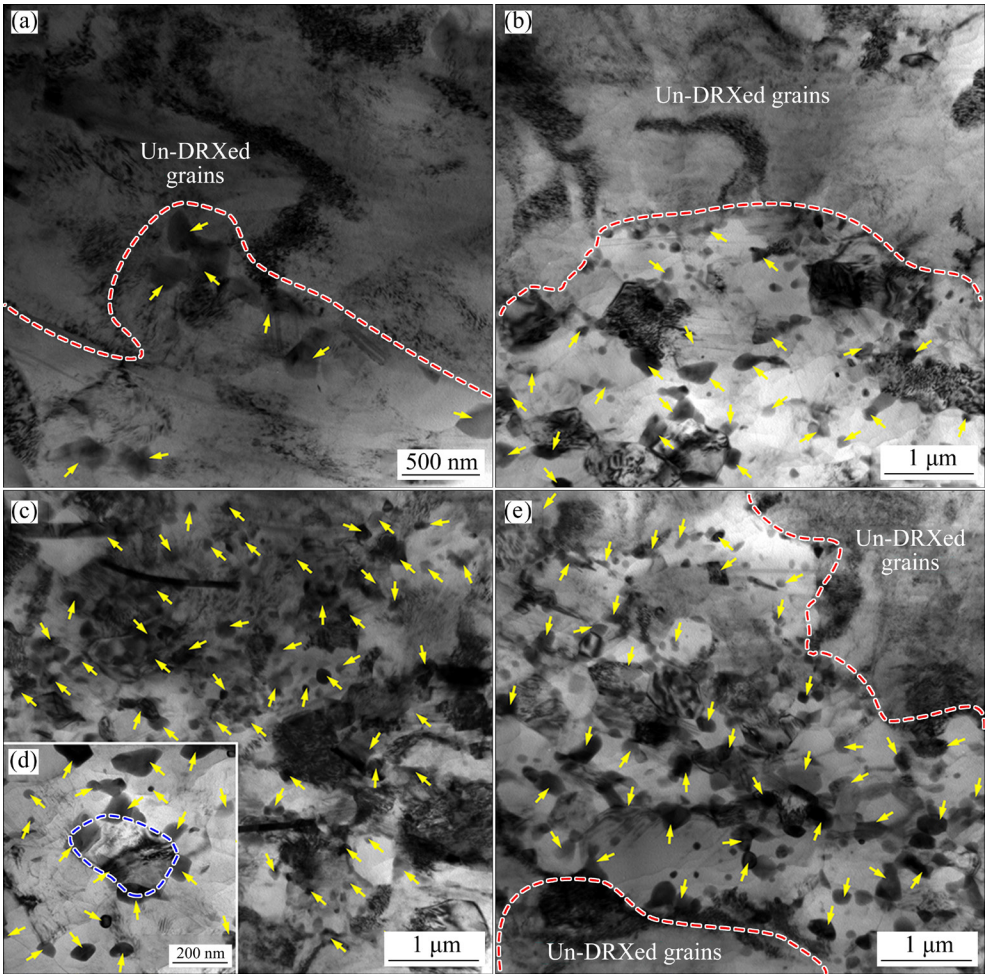

Fig. 13 TEM bright-field images of different samples after extrusion: (a) SE sample; (b) UAE sample; (c, d) PAE sample; (e) OAE sample

3.4 Mechanical properties of different samples during extrusion deformation

Figure 14 shows the RT tensile properties of different extruded samples. The comprehensive mechanical properties of the SE samples were the worst among all samples, and the yield strength (YS), UTS and EL were 336 MPa, 389 MPa and 7.4% respectively. Compared with the SE sample, the EL of the UAE sample was reduced by 0.9%, although its YS and UTS were increased by 43 MPa and 57 MPa, respectively. The PAE sample has the best tensile properties, and its YS, UTS and EL were 412 MPa, 482 MPa and 8.8% respectively. These results show that the strengths of samples prepared by a combination of pre-ageing treatment and extrusion deformation were significantly improved, but the elongation evolution law shows a fluctuating trend. The difference between tensile properties may be caused by various micro-structures.

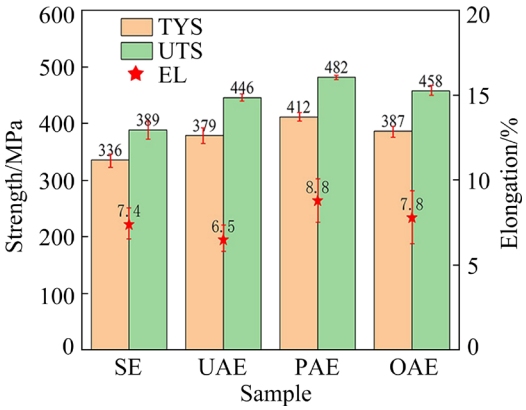

Fig. 14 RT tensile properties of different samples

4 Discussion

4.1 Effect of pre-heating treatment on precipitates

Pre-ageing treatment has attracted widespread attention from researchers, and preliminary studies have been conducted on Mg alloys such as AZ80, AZ91, Mg–8.32Sn–1.85Zn–0.17Mn, ZM61 and Mg−6Zn−1Gd−1Er. However, the effect of pre-heating treatment before deformation on the microstructure of pre-aged samples requires attention. PENG et al [31] explored the deformation behavior of ZK60 alloy with different states and found that the original microstructure (located in the grains and at the grain boundaries) of the pre-aged sample was transformed during the pre-heating process, which significantly affected subsequent recrystallization behavior. This indicates that it is more rigorous and scientific to investigate whether the original microstructure is transformed or stabilized in the thermal insulation treatment before deformation for subsequent research. In addition, studies on the ageing precipitation behavior of Mg−Gd−Y−Zn−Zr alloy showed that the ageing precipitation of the γ' phase or β'' (β') phase exhibited high thermal sensitivity, and these metastable phases underwent further transformations as the heating time or heating temperature was increased [9,25,42]. Therefore, it is necessary to explore the microstructure evolution of different pre-aged samples during the pre-heating process.

After pre-heating treatment, the types and sizes of the second phase of the three aged samples showed obvious differences. On the one hand, the metastable γ' and β'' phases of the UA sample underwent different transformations during the pre-heating process (Figs. 1(a−e)). The metastable β'' phase disappeared (without being coarsened and transformed into β phase) and the denser γ' phase was distributed in the original grains. The metastable precipitates were not monotonously coarsened and transformed during the pre-heating process according to the isothermal ageing precipitation sequence.

Previous studies on the effect of tensile temperature on the microstructure of Mg−9.5Gd−4Y−2.2Zn−0.5Zr (wt.%) alloy proved that the content of the newly formed γ' phase increased significantly as the tensile temperature was increased, while the β' phase gradually disappeared [9]. WANG et al [43] indicated that the β' phase was rapidly coarsened and transformed into β_1 phase, while the γ' phase had not yet undergone transformation during isothermal ageing at 225 °C. These results proved that the γ' phase has higher thermal stability than the β'' (β') phase, which may be attributed to the fact that more RE atoms improved the thermal stability of the γ' phase or transformation of the γ' phase requires more energy and RE atoms to form the new second phase. The tiny RE atom clusters (β'' phase) formed by segregation of RE atoms at the initial ageing stage were extremely unstable and easily annihilated during pre-heating due to the excessively high pre-heating temperature used (2.25 times the ageing temperature). Furthermore, our previous studies showed that the β particle

(distributed at grain boundaries or within grains) formed in PA samples can be attributed to coarsening transformation (rather than annihilation) of the β' phase after the pre-heating [20]. It is known that with extended ageing time (112 h), the coarser β' phase formed by further segregation of RE atoms had higher thermal stability than the β'' phase formed in the initial ageing stage (64 h). This showed that various metastable ageing precipitates (β'', β' and γ') evolved via different mechanisms during the pre-heating process. On the other hand, both PA and OA samples had β particles distributed at the grain boundaries and inside the grains after pre-heating treatment, but their quantity and size were slightly different. Obviously, compared with the OA sample, the PA sample had denser and finer β particles after the pre-heating treatment (Figs. 1(g, h)), which can be attributed to severe local segregation and aggregation of solute atoms due to the excessively long ageing time; this resulted in fewer nucleation sites and coarser precipitates in the OA sample [43,44]. Therefore, differences in the morphologies and quantities of particles in different extruded samples can be attributed to the original second phase of different samples after pre-heating treatment.

In summary, pre-heating treatment can significantly affect the original microstructures of pre-aged samples, which makes the research more scientific and rigorous by confirming the transformation law for the ageing metastable phase after pre-heating treatment. The precipitation behavior and strengthening effects of the ageing precipitates in the Mg−Gd−Y−Zn−Zr alloy during the isothermal post-ageing process (after deformation) become a current research focus, but the mechanism for evolution of metastable ageing precipitates during high temperature preheating is still unclear.

4.2 Effect of pre-ageing state on recrystallization behavior

4.2.1 Recrystallization nucleation of different samples

Many studies have proven that the original microstructure dominates the deformation behavior and mechanical properties of the alloy. PENG et al [45] studied the influence of second phase on the microstructure and mechanical properties of Mg−2.0Zn−1.5Mn (wt.%) alloy, which indicated that the dynamic synergistic effect of the PSN effect and pinning effect can be controlled by adjusting the types of initial second phase. KANG et al [32] confirmed that the second phase affected twinning behavior and texture evolution through dynamic precipitation and dissolution mechanisms. The EBSD results for different samples, shown in Figs. 2−12, indicated that the original microstructure significantly affected DRX behavior during the extrusion process. Research by WANG et al [23] showed that γ' phase can retard the recrystallization kinetics of Mg−Gd−Y−Zn−Mn alloy, which resulted in finer and sparse fine grains. Therefore, the densely distributed γ' phase inside the original grains of UA samples after pre-heating inhibited basal dislocation slips during the early extrusion stage, thereby inducing activation of many $\{10\bar{1}2\}$ tensile twins (lower critical resolved shear stress (CRSS) compared with non-basal slip systems). With further extrusion deformation, the twins gradually swallowed the parent grains to form new reoriented grains, which favored the initiation of dislocation slip. Therefore, numerous moving dislocations caused the twins to accumulate and entangle to form sub-grains; with further deformation, the sub-grains gradually transformed from LAGBs to HAGBs by absorbing more dislocations; finally, fine grains with random orientations were formed (Figs. 8(d) and (e)), such as in a typical CDRX mechanism. ZHAO et al [46] proved that twin boundaries effectively hindered the movement of dislocations, and their interaction was conducive to formation of isolated fine grains, which is a typical DDRX mechanism. These results indicated that the original grains with twins promoted grain refinement through the TDRX mechanism. In addition, a comparison between Fig. 3 and Fig. 7 shows that the misorientation angle increased from 4° to 14° and the grain boundaries changed from smooth to jagged in the non-twinned original grains with further deformation, indicating that dislocation slips were gradually activated to initiate the CDRX and DDRX mechanisms. The $\{10\bar{1}2\}$ twin-induced recrystallization behavior made limited contribution to grain refinement due to the high activation of its grain boundaries [47,48]. Therefore, with further accumulation of strain, the quantity of fine grains in the UAE sample gradually increased but the extent

of improvement was limited. Finally, the volume fraction of fine grains was 17.4%, which was the lowest among all samples.

In contrast, it is obvious that the PAE and OAE samples had different original microstructures, resulting in significant differences in their recrystallization behavior during the extrusion deformation. ZHONG et al [49] proved that particles promoted the formation of fine grains via the PSN mechanism. The interactions of numerous particles (distributed inside the original grain and at the grain boundary) with dislocations significantly promoted the accumulation of dislocations around the particles and the formation of LAGBs (marked by the red arrows in Figs. 5(d) and (e)). The misorientation angle inside the original grains exceeded 25° (Fig. 6(j)), and the serrated grain boundaries with many LAGBs (marked by the red arrows in Figs. 6(e) and (h)) indicated the CDRX and DDRX mechanisms were activated. Therefore, compared with the UAE sample containing almost no fine grains (Fig. 3), many fine grains with random orientations (Figs. 6(f) and (g)) were distributed at the grain boundaries and within the grains of the PAE sample at the initial extrusion stage (20 mm) (Fig. 5 and Fig. 6). These results indicated that the activated DRX mechanisms operating at the initial extrusion stage of the PAE sample included PSN, CDRX and DDRX mechanisms. Surprisingly, the formation of HAGBs along the kink bands of the lamellar LPSO phase split the original grains into several isolated new grains with further deformation, which is defined as a kink band-induced dynamic recrystallization (KDRX) mechanism. ZHOU et al [50] proved that the lamellar LPSO phase formed new grain boundaries at the kink bands to promote grain refinement through the CDRX mechanism as the strain was increased. MENG et al [34] revealed the evolution mechanism of the LPSO phase during deformation, and showed that the orientation deflection angle of the newly formed grains (located between the kinked bands) was closely related to the kink angle, which was consistent with the EBSD and SEM results of *R*1 and *R*2 regions in Fig. 10. Obviously, the above discussion showed that the interactions of kink bands in the lamellar LPSO phase and dislocations caused concentrated stress during the extrusion deformation process; after further deformation, LAGBs formed by dislocation rearrangement and climbing gradually were transformed into HAGBs through further capture of dislocations; finally, new grains were formed (KDRX). The sizes and orientations of the newly formed grains were determined by the width of the kink bands and the kink angle. In the end, the volume fraction of fine grains in the PEA sample reached 89.7%, which was much higher than that of the UAE sample. To enhance the understanding of various second phases and their effects on recrystallization behavior, a schematic diagram of the DRX behavior in different samples is shown in Fig. 15.

In summary, there are significant differences in the interactions between dislocations and the original second phases with various morphologies and quantities; this can transform DRX behavior during the extrusion process, thereby tailoring the microstructure of the extruded sample.

4.2.2 Recrystallization growth behavior of different samples

The recrystallization process includes two stages of grain nucleation and grain growth. EBSD observations showed that different pre-ageing states affected the volume fraction of fine grains by modifying the DRX behavior during extrusion deformation and also caused slight differences in the average grain sizes of the fine grains in different samples after extrusion. YU et al [51] also proved that the precipitates promoted grain refinement through the PSN mechanism and also inhibited grain boundary migration through the pinning effect. According to the interaction between the particle phase and the grain boundaries [52]:

$$v=M_0\exp[-Q/(RT)](P_{\mathrm{D}}^{\mathrm{Rex}}-P_{\mathrm{z}}-P_{\mathrm{c}}) \quad (1)$$

where v is the boundary migration rate, M_0 is the boundary migration constant, Q is the apparent activation energy, R is the molar gas constant, T is the deformation temperature, $P_{\mathrm{D}}^{\mathrm{Rex}}$ is the recrystallization driving force, P_{z} is the Zener pressure, and P_{c} is the boundary curvature. This indicates that the migration rate of the grain boundaries will be delayed as the Zener pressure (provided by the particles) increases. According to the Zener pressure formula [52]:

$$P_{\mathrm{z}}=3f_{\mathrm{v}}\gamma/(2r) \quad (2)$$

where f_{v} is the volume fraction of the particle phase, γ is the shear strain, and r is the average radius of

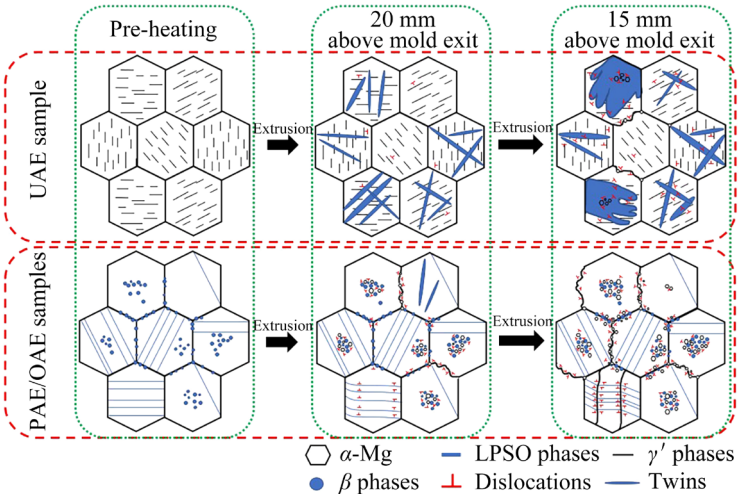

Fig. 15 Schematic diagram of DRX behavior in different samples during extrusion process

the particle phase. This formula shows that denser and finer particles hinder grain boundary migration more effectively. Compared with the pre-aged samples, the average grain size of the fine grains in the SE sample with the lowest volume fraction of particle phase (1.51%) was the largest (~2.7 μm), which indicated that the SE sample lacked enough particles to hinder further growth by fine grains. The increase in the volume fraction of the particle phase (increase in Zener pressure P_z) inhibited grain boundary migration of the fine grains, and the average grain size was significantly reduced. Compared with the SE samples, the average grain size of the fine grains in the pre-aged samples was reduced from ~2.7 to ~2.3 μm. Unexpectedly, the UAE sample had the finest recrystallized grains, which may be related to the distribution area of the fine grains. ZHANG et al [47,53] showed that finer recrystallized grains distributed along the grain boundaries of coarsely deformed grains were attributable to the stress concentration generated by the high-density dislocations at the grain boundaries of deformed grains, which inhibited the coarsening for fine grains. Therefore, the cumulative contribution of the pinning effect for fine particles and the hindering effect for deformed grains made the average grain size of fine grains in the UAE sample (mainly distributed around the deformed grains) be approximately1.9 μm.

4.3 Effect of microstructure on mechanical properties

The mechanical properties of alloy materials are closely related to the microstructure. Previous studies have shown that improvements in the mechanical properties of pre-aged samples compared with solution samples are attributable to contributions form precipitation strengthening and grain boundary strengthening mechanisms [39]. DRX behavior and microstructural evolution of different pre-aged samples were discussed in detail above. However, the reasons for differences in the mechanical properties of different pre-aged samples considered in this work were still unclear: the strength was significantly improved, but the ductility fluctuated. The differences in strengthening mechanisms for different pre-aged samples mainly included: dislocation strengthening (σ_d), texture strengthening (σ_t), grain boundary strengthening (σ_g) and precipitation strengthening (σ_p), which excluded solution strengthening with the same contribution in different samples (alloy composition and deformation process were consistent).

The interactions between dislocations can hinder movement to improve strength. Formation of the fine grain region consumed numerous dislocations, so the contribution of the dislocation strengthening mechanism mainly affected the deformed grain region. Therefore, the contribution value of the dislocation strengthening mechanism (σ_d) can be calculated with the following formula [54]:

$$\sigma_{\mathrm{d}} = f_{\text{un-DRXed}} M\alpha Gb\sqrt{\rho_{\text{un-DRXed}}} \tag{3}$$

where $f_{\text{un-DRXed}}$ is the volume fraction of un-DRXed (deformed grain) region, M(=2.5) is the Taylor factor,

α is a constant (0.2 for Mg alloys), G is the shear modulus (16.6 GPa for Mg alloys), b is amplitude of Burger vector (0.321 nm for Mg alloys), and $\rho_{\text{un-DRXed}}$ is the dislocation density of the un-DRXed region (1×10^{14} m^{-2} for Mg alloys). Therefore, the dislocation strengthening contributions of UAE, PAE and OAE samples were calculated according to the above formula to be 30.8, 3.84 and 18.5 MPa, respectively.

The critical resolved shear stress (CRSS) for dislocation slip in Mg alloys is determined by the Schmid factor (SF), which is closely related to the grain orientation (texture). The HCP structure of the Mg alloys leads to (0001)$\langle 11\bar{2}0\rangle$ basal slips with the lowest CRSS as the dominant deformation mechanism under RT tension. Therefore, the formula for calculating the contribution of the texture strengthening mechanism (σ_t) is as follows [55]:

$$\sigma_t=0.3\sigma_0/m \tag{4}$$

where m is the average SF value, and σ_0 is a constant (approximately 46.5 MPa for Mg alloys). The (0001)$\langle 11\bar{2}0\rangle$ SF_{ave} values of different samples are provided in Table 2. Therefore, the texture strengthening contributions for UAE, PAE and OAE samples were calculated to be 139.5, 58.1 and 73.4 MPa, respectively (Table 3).

The grain boundary strengthening mechanism operates when grain boundaries hinder the movement of dislocations, leading to the improvement of the performance. Therefore, the Hall−Petch relationship only considers the contribution of the grain boundary strengthening mechanism (σ_g) of the fine grain region, and its formula was as follows [8]:

$$\sigma_g=f_{DRX}kd_{DRX}^{-1/2} \tag{5}$$

where f_{DRX} is the volume fraction of the recrystallized grain region, k is a constant (164 MPa for Mg alloys), and d_{DRX} is the average grain size of the recrystallized grains. The grain boundary strengthening contribution for the UAE, PAE and OAE samples were calculated as 20.7, 99.2 and 53.6 MPa, respectively (Table 3).

Many studies have confirmed that strength improvement in an alloy occurs through particles hindering the dislocation slips along with the cut-through mechanism or the bypass mechanism, the Orowan mechanism, which requires additional energy. The accumulated dislocations surrounding particles further hinder subsequent movement of dislocations, which also leads to an increase in strength. The contribution of the particle phase (σ_p) was calculated according to the following formula for the Orowan strengthening mechanism [56]:

$$\sigma_p=\frac{MGb}{2\pi d_p\left[\left(\frac{1}{2f_p}\right)^{1/3}-1\right]\sqrt{1-v}}\ln\left(\frac{d_p}{b}\right) \tag{6}$$

where d_p is the particle phase diameter ($d_p=\sqrt{LW}$, L and W are the length and width of particle phase, respectively), f_p is the volume fraction of particle phase, and v is Posisson ratio (v=0.35). The d_p and f_p of the particle phase for different samples are summarized in Table 2. Therefore, the calculated contributions of precipitation strengthening for the UAE, PAE and OAE samples were 75.5, 176.8 and 128.6 MPa, respectively (Table 3).

The contribution values of various strengthening mechanisms for different pre-aged samples are summarized in Table 3. The effect of the strengthening mechanism for all samples can be expressed as follows: $\sigma=\sigma_d+\sigma_t+\sigma_g+\sigma_p$, and the results were 266.5 MPa (UAE sample), 337.9 MPa (PAE sample) and 274.1 MPa (OAE sample). These four strengthening mechanisms made the lowest contribution in the UAE sample, and the highest contribution in the PAE sample, which is consistent with the strength evolution law in Fig. 14. It is Obvious that the contributions of various strengthening mechanisms in the three samples

Table 2 (0001)$\langle 11\bar{2}0\rangle$ SF_{ave}, d_p and f_p of particle phase of UAE, PAE and OAE samples

Sample	(0001)$\langle 11\bar{2}0\rangle$ SF_{ave}	f_p/%	d_p/nm
UAE	0.1	3.91	161.91
PAE	0.24	10.5	136.34
OAE	0.19	8.22	152.7

Table 3 Contribution values of various strengthening mechanisms of UAE, PAE and OAE samples

Sample	σ_d/MPa	σ_t/MPa	σ_g/MPa	σ_p/MPa
UAE	30.8	139.5	20.7	75.5
PAE	3.8	58.1	99.2	176.8
OAE	18.5	73.4	53.6	128.6

were different due to differences in their microstructures. The UAE sample with the highest volume fraction of deformed grains had the strongest texture strengthening effect and dislocation strengthening effect; they reached 139.5 and 30.8 MPa, respectively, which indicated that deformed grains significantly increased the strength of the Mg alloy. However, inconsistent deformation between different deformation regions usually causes the initiation and propagation of cracks, especially for deformed grains with high local stress concentrations [57]. In tensile fracture of the UAE sample (Fig. 16), the cracks formed inside the deformed grains were rougher (marked by the blue arrows in Fig. 16) than those in other regions (marked by the yellow and green arrows in Fig. 16). Premature initiation and propagation of cracks limited further improvements in ductility [58], which was why the UAE sample exhibited the worst ductility. Interestingly, compared with the UAE sample, the PEA and OAE samples with higher strengths had lower contributions from dislocation strengthening and texture strengthening, which indicated that grain boundary strengthening and precipitation strengthening, their dominant strengthening mechanisms, made stronger contributions. The contributions of grain boundary strengthening and precipitation strengthening mechanisms in the PEA sample, which exhibited the densest and finest particles and the highest volume fraction of recrystallized grains, were 99.2 and 176.8 MPa, respectively, which were the highest of all samples. Incredibly, the UAE sample with the finest recrystallized grains had the worst grain boundary strengthening effect (only 20.7 MPa), which showed that the synergistic effects of size and volume fraction of recrystallized grains improved the strength more effectively. In addition, previous studies showed that a homogeneous microstructure with densely distributed particles could accommodate more dislocations during the tensile process, which inhibited premature initiation and propagation of cracks [59]. This is consistent with the higher ductility of the PAE and OAE samples seen in this study. The fracture morphologies of different samples, shown in Fig. 17, also supported this conclusion: PAE samples had the best ductility. Figure 17 shows that the fracture morphology of the UAE sample consists of cleavage planes (marked by the yellow arrows in Fig. 17), tear ridges (marked by the green arrows in Fig. 17) and few dimples (marked by the blue arrows in Fig. 17), which is a typical quasi-brittle fracture mode. In contrast, the fracture morphologies of the PAE and OAE samples were mostly composed of dimples, indicating that the cleavage mode was gradually converted to ductile fracture. In addition, the particle phase distributions around the dimples can be seen from the higher magnification images of the fracture morphologies for the three samples (Figs. 17(b, d, f); these distributions may cause the samples to absorb more energy before fracture to improve ductility during the tensile process. In summary, differences in the tensile properties of the three pre-aged extruded samples are attributed to different contributions of strengthening mechanisms caused by different microstructures.

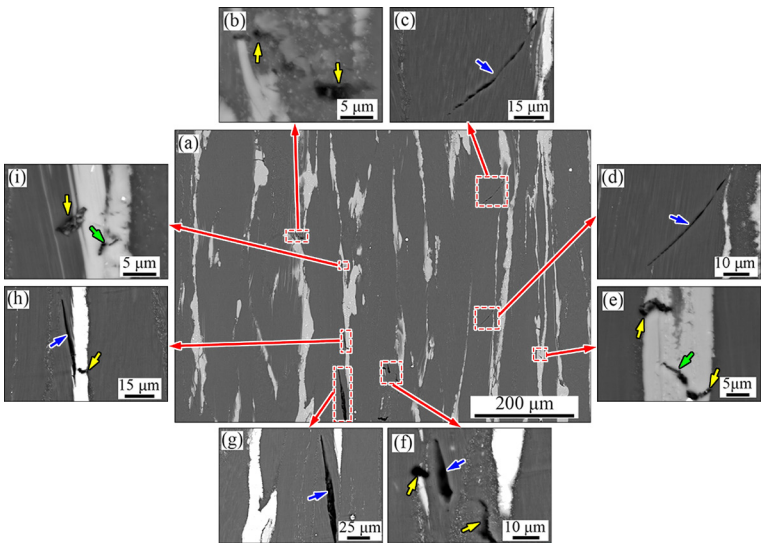

Fig. 16 SEM images showing tensile fracture characteristics of UAE sample

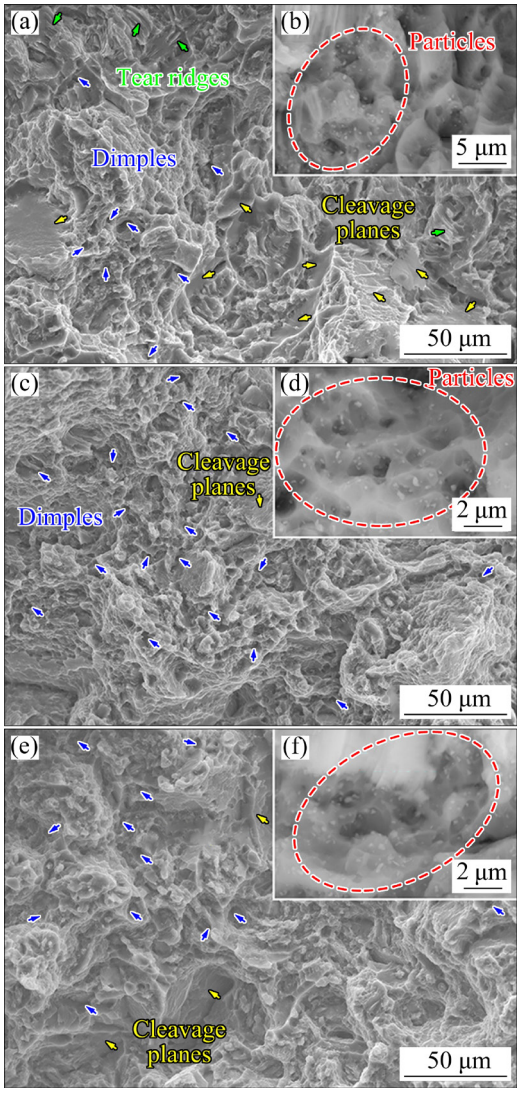

Fig. 17 SEM images showing fracture morphologies of different samples: (a, b) UAE sample; (c, d) PAE sample; (e, f) OAE sample

5 Conclusions

(1) Needle γ' phase was distributed inside the grains of the UA samples, while lamellar LPSO phase was distributed in PA and OA samples. In particular, numerous Mg_5RE particles were distributed inside the grains and at the grain boundaries of the PA and OA samples, which were denser and finer in the PA sample.

(2) The ingot condition before extrusion significantly affects the microstructure and mechanical properties of the as-extruded Mg−Gd−Y−Zn−Zr alloy. The extruded PAE samples with denser particle phase distribution exhibit finer and homogeneous microstructures, thus exhibiting better mechanical properties.

(3) The original second phase particles have a significant PSN effect during extrusion deformation, which effectively improves the grain refinement effect. The inhibition of dislocation slips by dense needle-like γ' induces twinning to be easily activated at the early stage deformation, delaying DRX nucleation and weakening the grain refinement effect.

(4) Texture strengthening and dislocation strengthening mechanisms dominated in UAE samples with typical bimodal microstructures. However, the contributions of grain boundary strengthening and precipitation strengthening mechanisms for PAE and OAE samples significantly exceeded those of UAE sample, which gave the PAE and OAE samples excellent mechanical properties.

CRediT authorship contribution statement

Jian XU: Writing –Original draft, Review & editing, Software, Data curation; **Jie ZHENG:** Software, Data curation, Writing – Original draft; **Wan-er LIU:** Data curation; **You-wang HUANG:** Software; **Zhao-ming YAN:** Methodology, Conceptualization; **ZHANG Zhi-min:** Funding acquisition; **Qiang WANG**: Visualization; **Yong XUE:** Methodology, Conceptualization.

Declaration of competing interest

The authors declare that they have no known competing financial interests or personal relationships that could have appeared to influence the work reported in this paper.

Acknowledgments

This work was supported by the National Natural Science Foundation of China (No. 52075501), and Fundamental Research Program of Shanxi Province, China (No. 20210302124206)

References

[1] PENG Yong-gang, DU Zhi-wei, LIU Wei, LI Yong-jun, LI Ting, HAN Xiao-lei, MA Ming-long, PANG Zheng, YUAN Jia-wei, SHI Guo-liang. Evolution of precipitates in Mg−7Gd−3Y−1Nd−1Zn−0.5Zr alloy with fine plate-like 14H-LPSO structures aged at 240 °C [J]. Transactions of Nonferrous Metals Society of China, 2020, 30(6): 1500−1510.

[2] SONG Jiang-feng, CHEN Jing, XIONG Xiao-ming, PENG Xiao-dong, CHEN Dao-lun, PAN Fu-sheng. Research

advances of magnesium and magnesium alloys worldwide in 2021 [J]. Journal of Magnesium and Alloys, 2022, 10(4): 863−898.

[3] WU Guo-hua, WANG Cun-long, SUN Ming, DING Wen-jiang. Recent developments and applications on high-performance cast magnesium rare-earth alloys [J]. Journal of Magnesium and Alloys, 2021, 9(1): 1−20.

[4] LIANG Min-jie, ZHENG Jie, LIU Huan, YAO Bao-xing. Microstructure and mechanical properties of AZ31 alloy prepared by cyclic expansion extrusion with asymmetrical extrusion cavity [J]. Transactions of Nonferrous Metals Society of China, 2022, 32(1): 122−133.

[5] CHEN Xiang, WANG Wei-zhang, ZHANG Jun-lei, HUANG Guang-sheng, LIU Shuai-shuai, TANG Ai-tao, JIANG Bin, PAN Fu-sheng. Tailoring AZ91 laminates for combination of strength and ductility [J]. Transactions of Nonferrous Metals Society of China, 2021, 31(12): 3703−3718.

[6] LIU Wei, WU Bo-qiang, LIU Hai-rong, LIU Rang-su, MO Yun-fei, TIAN Ze-an, HOU Zhao-yang, XI Ting-fei, WAN Zhi-yi, HUANG Chang-xiong, CHEN Xin. Simulation on microstructure evolution and mechanical properties of Mg−Y alloys: Effect of trace Y [J]. Transactions of Nonferrous Metals Society of China, 2022, 32(3): 812−823.

[7] XIN T Z, ZHAO Y H, MAHJOUB R, JIANG J X, YADAV A, NOMOTO K, NIU R M, TANG S, JI F, QUADIR Z, MISKOVIC D, DANIELS J, XU W Q, LIAO X Z, CHEN L Q, HAGIHARA K, LI X Y, RINGER S, FERRY M. Ultrahigh specific strength in a magnesium alloy strengthened by spinodal decomposition [J]. Science Advances, 2021, 7(23): eabf3039.

[8] WANG Jun-kai, LIU Chu-ming, JIANG Shu-nong, WAN Ying-chun, CHEN Zhi-yong. Effect of heat treatment on the microstructure and mechanical properties of a multidirectionally forged Mg−Gd−Y−Zn−Zr−Ag alloy [J]. Journal of Magnesium and Alloys, 2023, 11(6): 2042−2053.

[9] ZHENG Jie, YAN Zhao-ming, JI Jin-sheng, SHI Yu-sha, ZHANG Heng, ZHANG Zhi-min, XUE Yong. Effect of heat treatment on mechanical properties and microstructure evolution of Mg−9.5Gd−4Y−2.2Zn−0.5Zr alloy [J]. Journal of Magnesium and Alloys, 2022, 10(4): 1124−1132.

[10] YANG Yan, XIONG Xiao-ming, CHEN Jing, PENG Xiao-dong, CHEN Dao-lun, PAN Fu-sheng. Research advances in magnesium and magnesium alloys worldwide in 2020 [J]. Journal of Magnesium and Alloys, 2021, 9(3): 705−747.

[11] WANG Bo-ning, WANG Feng, WANG Zhi, LIU Zheng, MAO Ping-li. Fabrication of fine-grained, high strength and toughness Mg alloy by extrusion−shearing process [J]. Transactions of Nonferrous Metals Society of China, 2021, 31(3): 666−678.

[12] DING Zhi-bing, ZHANG Shuai, ZHAO Yu-hong, CHEN Dong-rui, ZOU Li-hua, CHEN Zhi-gang, GUO Wen-min, SU Zai-jun, HOU Hua. Effect of Al addition on microstructure and mechanical properties of Mg−Gd−Zn alloys [J]. Transactions of Nonferrous Metals Society of China, 2022, 32(3): 824−837.

[13] FAN Wen-xue, BAI Yu, LI Guang-yang, CHANG Xing-yang, HAO Hai. Enhanced mechanical properties and formability of hot-rolled Mg–Zn–Mn alloy by Ca and Sm alloying [J]. Transactions of Nonferrous Metals Society of China, 2022, 32(4): 1119−1132.

[14] ZHANG Zhi, ZHANG Jing-huai, WANG Jun, LI Ze-hua, XIE Jin-shu, LIU Shu-juan, GUAN Kai, WU Rui-zhi. Toward the development of Mg alloys with simultaneously improved strength and ductility by refining grain size via the deformation process [J]. International Journal of Minerals Metallurgy and Materials, 2021, 28(1): 30−45.

[15] ZHU Yu-lin, LIU Fei-ya, XIN Ren-long, SONG Bo, LIU Qing. Influence of aging prior to extrusion on the microstructure and mechanical properties of an extruded AZ91 alloy [J]. Advanced Engineering Materials, 2020, 22(7): 2000201.

[16] ZHU Yu-lin, LIU Fei-ya, XIN Ren-long, SONG Bo, LIU Qing. Improving mechanical properties of an AZ91 alloy by properly combining aging treatment and torsion deformation [J]. Materials Science and Engineering A, 2020, 779: 139156.

[17] ZHU Yu-lin, LIU Fei-ya, SONG Bo, XIN Ren-long, Coupling pre-aging treatment and side-rolling to improve the mechanical properties of AZ80 alloys [J]. Materials Science and Engineering A, 2020, 779: 139158.

[18] WANG Li-fei, ZHANG Zheng-yong, ZHANG Hua, WANG Hong-xia, SHIN Kwang-seon. The dynamic recrystallization and mechanical property responses during hot screw rolling on pre-aged ZM61 magnesium alloys [J]. Materials Science and Engineering A, 2020, 798: 140126.

[19] YANG Zhen-quan, MA Ai-bin, JIANG Jing-hua, SUN Jia-peng, LIU Huan, SONG Dan, WU Yun, YUAN Yu-chun, JIANG Jing-hua, SUN Jia-peng. Managing strength and ductility in AZ91 magnesium alloy through ECAP combined with prior and post aging treatment [J]. Materials Characterization, 2019, 152: 213−222.

[20] ZHENG Jie, CHEN Zhe, YAN Zhao-ming, ZHANG Zhi-min, WANG Qiang, XUE Yong. Preparation of ultra-high strength Mg−Gd−Y−Zn−Zr alloy by pre-ageing treatment prior to extrusion [J]. Journal of Alloys and Compounds, 2022, 894: 162490.

[21] YU Zi-jian, LIU Lin-lin, MANSOOR Adil, LIU Ke, LI Shu-bo, DU Wen-bo. Microstructures and mechanical properties of as-extruded Mg–8Gd–2Y–1Zn–6Li alloy [J]. Journal of Alloys and Compounds, 2021, 864: 158826.

[22] YU Zi-jian, HUANG Yuan-ding, MENDIS C L, HORT N, MENG Jian. Microstructural evolution and mechanical properties of Mg–11Gd–4.5Y–1Nd–1.5Zn–0.5Zr alloy prepared via pre-ageing and hot extrusion [J]. Materials Science and Engineering A, 2015, 624: 23−31.

[23] WANG Kui, DOU Xiao-xu, WANG Jing-feng, HUANG Yuan-ding, GAVRAS S, HORT N, LIU Shi-jie, HU Hao, WANG Jin-xing, PAN Fu-sheng. Achieving enhanced mechanical properties in Mg−Gd−Y−Zn−Mn alloy by altering dynamic recrystallization behavior via pre-ageing treatment [J]. Materials Science and Engineering A, 2020, 790: 139635.

[24] HONMA T, OHKUBO T, KAMADO S, HONO K. Effect of Zn additions on the age-hardening of Mg−2.0Gd−1.2Y−0.2Zr alloys [J]. Acta Materialia, 2007, 55(12): 4137−4150.

[25] XU C, ZHENG M Y, WU K, WANG E D, FAN G H, XU S W, KAMADO S, LIU X D, WANG G J, LV X Y. Effect of

ageing treatment on the precipitation behaviour of Mg–Gd–Y–Zn–Zr alloy [J]. Journal of Alloys and Compounds, 2013, 550: 50−56.

[26] SUN W T, QIAO X G, ZHENG M Y, ZHAO X J, CHEN H W, GAO N, STARINK M J. Achieving ultra-high hardness of nanostructured Mg−8.2Gd−3.2Y−1.0Zn−0.4Zr alloy produced by a combination of high pressure torsion and ageing treatment [J]. Scripta Materialia, 2018, 155: 21−25.

[27] ZHOU Xiao-jie, YAO Yuan, ZHANG Jian, CHEN Xiao-min, HUANG Wei-ying, PAN Jing, WANG Hao-ran, WENG Mao-peng. A high-performance Mg−4.9Gd−3.2Y−1.1Zn−0.5Zr alloy via multidirectional forging after analyzing its compression behavior [J]. Journal of Materials Science & Technology, 2021, 70: 156−167.

[28] XUE Xiao-yu, WU Yu-juan, SU Ning, HENG Xiang-wen, DENG Qing-chen, CHANG Zhi-yu, PENG Li-ming. High-strength GWZ1031K alloy with gradient structure induced by surface mechanical attrition treatment [J]. Materials Characterization, 2020, 170: 110701.

[29] XU Wen-long, YU Jian-min, JIA Lei-chen, WU Guo-qin, ZHANG Zhi-min. Deformation behavior of Mg−13Gd−4Y−2Zn−0.5Zr alloy on the basis of LPSO kinking, dynamic recrystallization and twinning during compression-torsion [J]. Materials Characterization, 2021, 178: 111215.

[30] WANG Kui, WANG Jing-feng, HUANG Song, DOU Xiao-xu, WANG Jin-xing, WANG Cun-long. Formation of an abnormal texture in Mg−Gd−Y−Zn−Mn alloy and its effect on mechanical properties by altering extrusion parameters [J]. Materials Science and Engineering A, 2022, 831: 142270.

[31] PENG Peng, ZHANG Kun-min, SHE Jia, TANG Ai-tao, ZHANG Jian-yue, SONG Kai, YANG Qing-shan, PAN Fu-sheng. Role of second phases and grain boundaries on dynamic recrystallization behavior in ZK60 magnesium alloy [J]. Journal of Alloys and Compounds, 2021, 861: 157958.

[32] KANG Wei, LU Li-wei, FENG Long-biao, LU Feng-chi, GAN Chun-lei, LI Xiao-hui. Effects of pre-aging on microstructure evolution and deformation mechanisms of hot extruded Mg–6Zn–1Gd–1Er Mg alloys [J]. Journal of Magnesium and Alloys, 2023, 11(1): 317−328.

[33] CUI Chao, HE Jian, WANG Wen-ke, CHEN Wen-zhen, ZHANG Wen-cong, CHEN Xue-min, HOU Jia-bin. Unveiling the microstructure evolution based on deformation mechanisms and dynamic recrystallization in as-extruded AZ31 Mg alloys during uniaxial compression [J]. Journal of Alloys and Compounds, 2022, 894: 162417.

[34] MENG Ying-ze, YU Jian-min, LIU Kai, YU Huis-heng, ZHANG Fan, WU Yao-jin, ZHANG Zhi-min, LUO Ni-na, WANG Hong-hai. The evolution of long-period stacking ordered phase and its effect on dynamic recrystallization in Mg−Gd−Y−Zn−Zr alloy processed by repetitive upsetting-extrusion [J]. Journal of Alloys and Compounds, 2020, 828:154454.

[35] HAGIHARA K, YOKOTANI N, UMAKOSHI Y. Plastic deformation behavior of $Mg_{12}YZn$ with 18R long-period stacking ordered structure [J]. Intermetallics, 2010, 18(2): 267−276.

[36] WANG J, FERDOWSI M R G, KADA S R, BABANIARIS S, HUTCHINSON B, LYNCH P A, BARNETT M R. Appearance of textures with a c-axis parallel to the extrusion direction in Mg alloys [J]. Scripta Materialia, 2022, 210:114422.

[37] JIN Xue-ze, XU Wen-chen, YANG Zhong-ze, YUAN Can, SHAN De-bin, TENG Bu-gang, JIN Bo-cheng. Analysis of abnormal texture formation and strengthening mechanism in an extruded Mg−Gd−Y−Zn−Zr alloy [J]. Journal of Materials Science & Technology, 2020, 45: 133−145.

[38] RAMEZANI S M, ZAREI-HANZAKI A, ABEDI H R, SALANDARI-RABORI A, MINARIK P. Achievement of fine-grained bimodal microstructures and superior mechanical properties in a multi-axially forged GWZ magnesium alloy containing LPSO structures [J]. Journal of Alloys and Compounds, 2019, 793: 134−145.

[39] ZHANG Jian-yue, PENG Peng, LUO Al-an, SHE Jia, TANG Ai-tao, PAN Fu-sheng. Dynamic precipitation and enhanced mechanical properties of ZK60 magnesium alloy achieved by low temperature extrusion [J]. Materials Science and Engineering A, 2022, 829: 142143.

[40] SU Ning, WU Yu-juan, DENG Qing-chen, CHANG Zhi-yu, WU Qian-ye, XUE Yan-ting, YANG Kun, CHEN Qiang, PENG Li-ming. Synergic effects of Gd and Y contents on the age-hardening response and elevated-temperature mechanical properties of extruded Mg−Gd(−Y)−Zn−Mn alloys [J]. Materials Science and Engineering A, 2021, 810: 141019.

[41] ZHANG Yu, RONG Wei, WU Yu-juan, PENG Li-ming. Tuning texture and precipitation using Y/Gd atomic ratio in iso-concentration Mg–Y–Gd–Ag–Zr extruded alloys [J]. Materials Characterization, 2020, 167: 110473.

[42] XU C, NAKATA T, QIAO X G, ZHENG M Y, WU K, KAMADO S. Effect of LPSO and SFs on microstructure evolution and mechanical properties of Mg−Gd−Y−Zn−Zr alloy [J]. Scientific Reports, 2017, 7: 40846.

[43] WANG Dan, FU Peng-huai, PENG Li-ming, WANG Ying-xin, DING Wen-jiang. Development of high strength sand cast Mg–Gd–Zn alloy by co-precipitation of the prismatic β' and β_1 phases [J]. Materials Characterization, 2019, 153: 157−168.

[44] XUE Xiong-wen, WANG Qiang, SONG Xiao-qian, YAN Zhao-ming, ZHENG Jie, GAO Chang, YIN Cai-hong, XUE Yong. Influence of a novel SPD technique together with heat treatment on the microstructural characteristics and hardness of Mg−13Gd−4Y−2Zn−0.5Zr alloys [J]. Materials Research Express, 2020, 7(12): 126518.

[45] PENG Peng, SHE Jia, TANG Ai-tao, ZHANG Jian-yue, SONG Kai, YANG Qing-shan, PAN Fu-sheng. A strategy to regulate the microstructure and properties of Mg−2.0Zn−1.5Mn magnesium alloy by tracing the existence of Mn element [J]. Journal of Alloys and Compounds, 2022, 890: 161789.

[46] ZHAO Feng, XIE Jin-hong, ZHU Yi-kun, LIU Qian-cheng, YE Tian, CHEN Lian-yang, SUO Tao, WANG Kai-xuan, WANG Tao, WANG Qing-yuan. A novel dynamic extrusion for microstructure tailoring and evading strength−ductility trade-off in AZ31 magnesium alloy [J]. Journal of Alloys and Compounds, 2021, 870: 159411.

[47] ZHANG Kai, ZHENG Jing-hua, HUANG Yan, PRUNCU C, JIANG Jun. Evolution of twinning and shear bands in

magnesium alloys during rolling at room and cryogenic temperature [J]. Materials & Design, 2020, 193: 108793.
[48] LU S H, WU D, CHEN R S, HAN E H. Reasonable utilization of $\{10\bar{1}2\}$ twin for optimizing microstructure and improving mechanical property in a Mg−Gd−Y alloy [J]. Materials & Design, 2020, 191: 108600.
[49] ZHONG Li-ping, WANG Yong-jian, DOU Yu-chen. On the improved tensile strength and ductility of Mg−Sn−Zn−Mn alloy processed by aging prior to extrusion [J]. Journal of Magnesium and Alloys, 2019, 7(4): 637−647.
[50] ZHOU Xiao-jie, LIU Chu-ming, GAO Yong-hao, JIANG Shu-nong, CHEN Zhi-yong. Improved workability and ductility of the Mg−Gd−Y−Zn−Zr alloy via enhanced kinking and dynamic recrystallization [J]. Journal of Alloys and Compounds, 2018, 749: 878−886.
[51] YU Zi-jian, XU Chao, MENG Jian, ZHANG Xu-hu, KAMADO S. Microstructure evolution and mechanical properties of as-extruded Mg−Gd−Y−Zr alloy with Zn and Nd additions [J]. Materials Science and Engineering A, 2018, 713: 234−243.
[52] HUANG Ke, MARTHINSEN K, ZHAO Qing-long, LOGÉ R E. The double-edge effect of second-phase particles on the recrystallization behaviour and associated mechanical properties of metallic materials [J]. Progress in Materials Science, 2018, 92: 284−359.
[53] ZHANG Kai, SHAO Zhu-tao, JIANG Jun. Effects of twin-twin interactions and deformation bands on the nucleation of recrystallization in AZ31 magnesium alloy [J]. Materials & Design, 2020, 194: 108936.
[54] LV Hao, LI Lu, WEN Zhuo-zhang, LIU Chun-rong, ZHOU Wei, BAI Xue, ZHONG Hui-ling. Effects of extrusion ratio and temperature on the microstructure and mechanical properties of Mg–Zn–Yb–Zr extrusion alloys [J]. Materials Science and Engineering A, 2022, 833: 142521.
[55] LI Guo-qiang, ZHANG Jing-huai, WU Rui-zhi, LIU Shu-juan, SONG Bo, JIAO Yu-feng, YANG Qiang, HOU Le-gan. Improving age hardening response and mechanical properties of a new Mg−RE alloy via simple pre-cold rolling [J]. Journal of Alloys and Compounds, 2019, 777: 1375−1385.
[56] YANG Zhen-quan, MA Ai-bin, XU Bing-qian, JIANG Jing-hua, SUN Jia-peng. Revealing the tensile anisotropy, tension–compression asymmetry, and strain-hardening behavior of a high-performance Mg–Gd–Ag alloy [J]. Journal of Alloys and Compounds, 2021, 868: 159238.
[57] XU C, FAN G H, NAKATA T, LIANG X, CHI Y Q, QIAO X G, CAO G J, ZHANG T T, HUANG M, MIAO K S, ZHENG M Y, KAMADO S, XIE H L. Deformation behavior of ultra-strong and ductile Mg−Gd−Y−Zn−Zr alloy with bimodal microstructure [J]. Metallurgical and Materials Transactions A, 2018, 49(5): 1931−1947.
[58] ZHENG Jie, CHEN Zhe, YAN Zhao-ming, ZHANG Zhi-min, XUE Yong. An alternating ageing-annealing process for enhancing strength and ductility of a Mg−Gd−Y−Zn−Zr alloy [J]. Materials Science and Engineering A, 2021, 828: 142103.
[59] SU Ning, XUE Xiao-yu, ZHOU Hui, WU Yu-juan, DENG Qing-chen, YANG Kun, CHEN Qiang, CHEN Bin, PENG Li-ming. Effects of nanoprecipitates and LPSO structure on deformation and fracture behaviour of high-strength Mg−Gd−Y−Zn−Mn alloys [J]. Materials Characterization, 2020, 165: 110396.

不同预时效挤压态 Mg−Gd−Y−Zn−Zr 合金的再结晶行为和强化机制

徐 健[1]，郑 杰[1]，刘莞尔[2]，黄有旺[3]，闫钊鸣[1]，张治民[1]，王 强[1]，薛 勇[1]

1. 中北大学 材料科学与工程学院，太原 030051；
2. 北京宇航系统工程研究所，北京 100076；
3. 北京长征飞行器研究所，北京 100071

摘 要：通过控制预时效时间制备 3 种不同状态的试样，研究不同预时效状态对挤压态 Mg−9.5Gd−4Y−2.2Zn−0.5Zr (质量分数，%)合金的动态再结晶行为(DRX)和性能的影响。结果表明，欠时效挤压(UAE)样品的细晶体积分数为 17.4%，而峰时效挤压(PAE)和过时效挤压(OAE)样品的细晶体积分数分别达到 89.7%和 50.4%。在晶粒内部和晶界处分布的致密、细小的 β 颗粒相通过粒子激发形核机制显著提高了形核位点和位错密度。然而，致密针状 γ'相抑制位错滑移，延迟 DRX 形核。PEA 和 OAE 样品中细小晶粒的差异归因于原始颗粒相的数量和尺寸的不同，而其拉伸性能的差异归因于不同的显微组织。由于晶界强化和析出强化机制的贡献更大，PAE 样品具有更优异的拉伸性能。

关键词：Mg−Gd−Y−Zn−Zr 合金；预时效处理；再结晶行为；强化机制；粒子刺激形核

(Edited by Wei-ping CHEN)